Exosomes-mediated molecular mechanisms underlying the transformation of ovarian tissue into a functional placental analogue in black rockfish (*Sebastes schlegelii*)

Authorship

Bing-Yan Zheng[1], Xiao-Jie Wang[1,2], Hai-Shen Wen[1], Yun Li[1], Jian-Shuang Li[1], Xin-Lin Yang[1], Li-Kang Lyu[1], Xin Qi[1, *].

1. Key Laboratory of Mariculture, Ministry of Education, Ocean University of China, Qingdao 266100, China
2. Yazhou Bay Innovation Institute, Hainan Tropical Ocean University, Sanya 572000, China

Funds:

This research was supported by the National Natural Science Foundation of China (32470555), Provincial Natural Science Foundation of Shandong (ZR2023QC009) and Municipal Natural Science Foundation of Qingdao (23-2-1-62-zyyd-jch).

*Corresponding author

Dr. Xin Qi, College of fishery, Ocean University of China, Qingdao, China

E-mail: qx@ouc.edu.cn[1]

[1] This research was supported by the National Natural Science Foundation of China (32470555), Provincial Natural Science Foundation of Shandong (ZR2023QC009) and Municipal Natural Science Foundation of Qingdao (23-2-1-62-zyyd-jch).

Running title: Ovarian exosome regulation in black rockfish placental analogue formation

Summary sentence: Ovarian exosomes deliver bioactive molecules with potential to regulate placental analogue formation of black rockfish

Highlights:

After fertilization in black rockfish, the primordial follicular tissue differentiates into a highly vascularized trophic capsule resembling a placenta.

Formation of the maternal placental analogue likely involves epithelial-mesenchymal interaction, angiogenesis, and immune responses.

Ovarian exosomes carry diverse functional proteins and RNAs associated with maternal placental analogue formation.

Exosomal transfer of *hgfb* mRNA elevates Hgfb expression in recipient cells and may drive ovarian tissue remodeling.

ABSTRACT

Viviparity has independently evolved multiple times in teleost, leading to diverse modes of maternal nutrient provisioning. In black rockfish (*Sebastes schlegelii*), embryos gain dry weight during gestation, with the presence of a placental connection that supports maternal-fetal nutrient transfer. Although prior studies have outlined the morphology and evolutionary convergence of the black rockfish placental analogue, its full architecture and underlying molecular mechanisms remain unresolved. Here, we show that the maternal component of the placental analogue, derived from ovarian follicular tissue, consists of a vascularized outer layer and a glandularized inner layer, organized into a sac-like structure, and at the molecular level, this transformation involves epithelial-mesenchymal interactions, angiogenesis, and immune responses. We observed exosome-like structures surrounding the placental analogue and isolated and characterized ovarian exosomes, suggesting active crosstalk between developing embryos and the maternal ovary underlying these changes. Subsequent proteomic and transcriptomic analyses revealed that they carry diverse functional cargos, including *hgfb* mRNA. We further showed that ovarian cells efficiently internalize exosomes, resulting in increased intracellular *hgfb* mRNA and subsequent Hgfb protein expression and secretion, which reprogram gene expression and promote placental development-related processes such as angiogenesis. Taken together, these findings elucidate the molecular mechanisms underlying ovarian placentation and angiogenesis during gestation in black rockfish, and are of significant theoretical relevance for understanding reproductive adaptations in fishes undergoing the evolutionary shift from oviparity to viviparity.

Keywords: Black rockfish; Placental analogue; Cell communication; Exosome; Exosome cargo

INTRODUCTION

Viviparity is a fundamental evolutionary innovation, representing maternal control over embryonic development by providing additional nutrients (Blackburn, 2015). Indeed, approximately 500 teleost species have evolved viviparity (Schindler & Hamlett, 1993), in which three modes of matrotrophy have been described: oophagy (adelphophagy), trophodermy, and placentotrophy, the latter being characterized by intimate apposition or fusion between maternal and fetal tissues that enables physiological exchange (Wourms et al., 1988). Consequently, viviparous teleost exhibit a wide range of structural and developmental modifications, including diverse placental forms follicular placenta (Grove & Wourms, 1994; Knight et al., 1985; Olivera-Tlahuel et al., 2019), buccal and branchial placentae (Di Cesare et al., 2023), and trophotaenial placentas (Lombardi & Wourms, 1985).

Despite their morphological diversity, all placentas carry out a conserved suite of essential functions, reflecting the convergent evolution of placental structures, which remain highly conserved at both physiological and molecular levels (Cross et al., 2003; Guernsey et al., 2020). This evolutionary trajectory is further marked by the accelerated diversification of genes implicated in in cell recognition, vesicular trafficking, and secretory pathways (Van Kruistum et al., 2021). Exosomes are small extracellular vesicles secreted by nearly all cells, including prokaryotes, indicating an ancient evolutionary origin and conserved roles in intercellular communication (Askenase, 2021). Growing evidence highlights the essential functions of

78 exosomes in mammalian gestation and placental development (Chen et al., 2023),
79 demonstrating their influence on decidualization, embryo implantation, and maternal immune
80 tolerance (Apostolov et al., 2025; Atay et al., 2011b; Ma et al., 2022; R. Ma et al., 2021). In
81 contrast, information on the exosome in viviparous teleost reproductive physiology is scarce
82 (Chen et al., 2024; Pan et al., 2025), particularly with regard to placental development.
83 Hepatocyte growth factor (HGF) has been shown to be expressed within villous mesenchyme,
84 where it contributes to the regulation of placental development (Clark et al., 1998). Notably,
85 HGF mRNA can be transferred to recipient cells via extracellular vesicles (Ju et al., 2015),
86 thereby augmenting their endogenous expression and enabling context-dependent functional
87 outcomes of HGF signaling.
88 Black rockfish, a viviparous teleost, exhibits asynchronous gonadal development and
89 undergoes gestation within the follicle (Mori et al., 2003). Although traditionally considered
90 lecithotrophic and retaining the high fecundity typical of oviparity, evidence for matrotrophy
91 comes from the increase in embryo dry weight during gestation (Boehlert & Yoklavich, 1984;
92 Wourms, 1991). Therefore, black rockfish may represent a transitional viviparous mode among
93 teleost (facultative matrotrophy, ovoviviparity), combining high fecundity with placentotrophy.
94 Recent studies have investigated the nutritional strategies and placental structures of black
95 rockfish, and suggest convergent evolution with other viviparous vertebrates (Tengfei et al.,
96 2021; Xu et al., 2022). However, practical challenge encountered is that black rockfish
97 placental malformations may impair embryonic development, resulting in markedly reduced
98 fry production (unpublished data), which underscores the critical importance of placental

function.

In this study, we investigated the morphological and transcriptomic changes underlying the development of the black rockfish placental analogue. Importantly, we isolated ovarian exosomes (ov-exos) and investigated their transported cargos and associated functions, such as *hgfb* (Hepatocyte growth factor b) mRNA, elucidating their role as messengers involved in placental-analogue formation. Overall, this work aims to provide a framework for elucidating gestation-related molecular regulatory mechanisms in black rockfish across histological, physiological, and molecular dimensions. Additionally, these findings advance our understanding of reproductive adaptations in ovoviviparous fishes and offer a valuable model for studying convergent evolution of viviparity in vertebrates.

MATERIALS AND METHODS

Sample collection

A total of 35 female black rockfish (over 3 years old) were collected from Nanshan Fisheries Market, Shandong Province, China, between April and May 2024. The animal experiments in this study were conducted following the protocols of the Institutional Animal Research and Ethics Committees of Ocean University of China before the initiation of the study. All procedures were performed in accordance with relevant guidelines and regulations.

All fish were anaesthetised using ethyl 3-aminobenzoate methanesulfonate (MS-222, 0.2 g/L; Beijing Green Hengxing Biotechnology, China), and then rapidly decapitated. Ovarian tissues were promptly dissected and divided for different analyses: half was immediately frozen in liquid nitrogen and stored at -80°C for molecular assays and exosome isolation; one-quarter

was fixed in 4% paraformaldehyde for histological examination; the remaining quarter was fixed in 2.5% glutaraldehyde for electron microscopy. Samples were grouped according to oocyte or embryonic developmental stages previously described (He et al., 2019): maturation (M, n=3), blastula (B, n=3), somite (S, n=3), and organogenesis (O, n=3).

Histochemical staining and cellular apoptosis detection

Following fixation, the ovarian tissue blocks were embedded in paraffin, and serially sectioned at 7 μm using a Leica RM2016 microtome (Germany). The sections were then deparaffinized, rehydrated and stained with haematoxylin and eosin (H&E), and examined under a light microscope (Olympus BX53, Tokyo, Japan). Cellular apoptosis was assessed using the TUNEL Apoptosis Detection Kit (FITC) (Yeasen Biotechnology Co., Ltd., China) according to the manufacturer's instructions.

In situ hybridization (ISH)

Paraffin-embedded ovarian tissues were processed for ISH using a standard protocol (Lyu et al., 2024). RNA probes were synthesized using a DIG RNA Labelling Kit (SP6/T7), Biotin RNA Labelling Mix, or Fluorescein RNA Labelling Mix (Roche Diagnostics, Germany). For dual-fluorescence in situ hybridization (DISH), probes were hybridized overnight at 55°C and then incubated with HRP-conjugated secondary antibodies and signal detection using Alexa Fluor 488, 594, or 647 tyramide kits (Invitrogen, USA). Sections were mounted with DAPI-containing Antifade Mounting Medium (Beyotime, China), imaged on an Olympus BX53F fluorescence microscope. BCIP/NBT detection was performed as previously described (Lyu et al., 2022).

Immunohistochemistry (IHC)

IHC was performed following a standard protocol (Wang et al., 2021). Sections were rehydrated and microwaved (in Sodium Citrate Buffer, pH=6) for antigen retrieval. After blocking, sections were incubated with primary antibody (anti-CD63, 1:400; anti-CD31, 1:2 000; anti-cMet (Cytoplasmic), 1:500; ProteinTech, China) overnight at 4°C, followed by incubation with Goat Anti-Mouse IgG(H+L), HRP Conjugated (1:200, Epizyme Biomedical Technology, China). Detection of antigen-antibody complexes was performed using the DAB Substrate Kit (Beijing Solarbio Science & Technology Co., Ltd.).

Ovarian vasculature perfusion and tissue clearing

As shown in Supplementary Figure S1, the intact ovary was excised from anesthetized fish. PBS was perfused until the effluent visibly cleared, followed by 4% PFA perfusion, and then 10 mL of a 10% India ink-2% preheated (40°C) gelatin mixture was manually injected using a 20 mL disposable syringe. After the gelatin had solidified, the tissue blocks were fixed in 4% PFA. Tissue clearing was performed following a previously described protocol with slight modifications (Susaki et al., 2014). Imaging was performed using a Nikon Eclipse Ti-U microscope (Nikon, Tokyo, Japan), and vascular branch numbers and vessel lengths were quantified using ImageJ 1.5e.

Isolation of ov-exos and RNase protection assay

Frozen ovarian tissue was thawed and minced until all pieces were of a homogeneous size. It was then incubated for 1h at 25°C with collagenase I (G-clone, China, 2 mg/mL) and DNase I (G-clone, China, 40 U/mL). Subsequently, the suspension was centrifuged at 400 ×***g*** for 10

minutes at 4°C to remove cells. After filtering through a 70 μm mesh, the supernatant was sequentially centrifuged at 2 000 ×***g*** for 20 min and 10 000 ×***g*** for 45 min at 4°C to remove cell debris and large vesicles, then passed through a 0.22 μm filter and ultracentrifuged at 100 000 ×***g*** for 70 min at 4°C (Optima XPN-100, Beckman Coulter, USA). The sediment was then resuspended in PBS and centrifuged again at 100 000 ×***g*** for 70 minutes at 4°C. The resulting pellet was resuspended in 200 μL PBS and stored at -80°C. To determine whether RNA is encapsulated within ov-exos, ov-exos were treated with RNase Ⅰ+Triton X-100, and the expression was measured by RT-qPCR.

Dynamic Light Scattering (DLS)

The size distribution of exosome was determined by dynamic light scattering experiments. Briefly, the ov-exos suspension was diluted 1 000-fold in particle-free PBS and measured using a Zetasizer Nano ZS (Malvern Instruments, UK). The data were then analysed using Zetasizer software.

Observation of ov-exos and placental analogue by electron microscopy

For ov-exos, the suspension was diluted 100-fold in PBS, dropped onto a copper grid, negatively stained with 2% Aqueous uranyl acetate solution and dried. The samples were then observed using a JEOL-1400Flash electron microscope (JEOL, Japan).

For the placental analogue, glutaraldehyde-fixed tissues were postfixed with osmium tetroxide, sectioned, and stained with uranyl acetate for ultrastructural observation using a JEOL-1400Flash transmission electron microscope (TEM). For scanning electron microscopy (SEM), tissues were dehydrated, critical-point dried, gold-coated, and imaged with a VEGA3

183 microscope (TESCAN, Czech).

184 **Isolation of proteins and immunoblotting**

185 Ovarian tissues, primary ovarian cells, and ov-exos suspensions were each lysed separately in
186 RIPA buffer (Beyotime, China). Ov-exos lysates were divided for mass spectrometry and
187 immunoblotting. Equal amounts of protein were electrophoresed on 10% SDS-PAGE gels
188 (Color PAGE Gel Rapid Preparation Kit, Epizyme Biomedical Technology, China), transferred
189 to PVDF membranes. Blocked membranes incubated overnight at 4 °C with primary antibodies:
190 Anti-CD63 (1:2 000, Abmart, China); anti-CD9 (1:2 000, HUABIO, China); anti-TSG101
191 (1:5 000), anti-Phospho-AKT (Ser473, 1:2000), anti-AKT (1:2 000) from ProteinTech, China;
192 anti-β-actin (1:10 000, Epizyme Biomedical Technology, China). Protein bands were detected
193 using HRP-conjugated goat anti-mouse/rabbit IgG (1:20 000, Epizyme, China) and the Omni-
194 ECL™ Femto Light Chemiluminescence Kit (Beyotime, China).

195 **Culture of primary ovarian cells and co-incubation with fluorescently-labeled ov-exos**

196 Ovarian matrix tissues from pregnant females were dissected, washed with PBS, minced, and
197 digested in trypsin-EDTA (Biosharp, China) for 20 min at room temperature. The suspension
198 was filtered through a 40 μm strainer, centrifuged at 400 ×***g*** at room temperature for 5 min, and
199 resuspended in L-15 medium (G-Clone, China) supplemented with 10% FBS and 1% PSG
200 (Penicillin-Streptomycin-Gentamicin Solution, Absin, China). Cells were cultured in six-well
201 plates at 25°C. Ov-exos were labeled with FluoExo® Exosome Tracing Staining Kit-Green
202 (Echo Biotech, China) according to the manufacturer's instructions. After removing free dye,

cells were incubated with labeled ov-exos for 24h, fixed in 4% PFA, counterstained with DAPI (G-Clone, China) and Actin-Tracker Red-555 (Beyotime, China).

Recombinant expression and angiogenic activity of Hgfb

The cDNA encoding the mature peptide of Hgfb was amplified and subcloned into a pET-28a expression vector with a C-terminal His-tag fusion. The recombinant vector was transformed into E. coli Rosetta (DE3) and was induced with 0.6 mM IPTG at 37°C for 6h. Cells were harvested and lysed by sonication, and inclusion bodies were isolated and denatured. Refolding was performed by gradual dilution, followed by purification using Ni-NTA affinity chromatography.

Primary ovarian microvascular cells were isolated from ovaries by collagenase/dispase digestion and cultured at 25°C for 48h. Following 12h of serum starvation, cells were treated with recombinant Hgfb for 6h, after which total RNA and protein were extracted.

RNA extraction, library construction, and Illumina sequencing

Total RNA was extracted from ov-exos and ovaries in different developmental stages using TRIzol reagent (Shandong Sparkjade Biotechnology Co., Ltd., China). The concentration and integrity of the total RNA were then assessed using an Agilent 2 100 pic600 nucleic acid analyser (Agilent Technologies, USA). RNA libraries of 12 ovarian stroma samples were prepared using the Fast RNA-seq Lib Prep Kit V2 (Abclonal, China) and sequenced on an Illumina NovaSeq X Plus platform with 150 bp paired-end reads. Exosomal lncRNA libraries were constructed using the AccuNext Stranded Single Cell & Low Input RNA-seq Kit (Accurate Biology, China) and sequenced on the same platform with 150 bp paired-end reads.

Exosomal small RNA libraries were prepared using the Small RNA Lib Prep Kit for Illumina V3 (Abclonal, China) and sequenced on an Illumina NovaSeq 6 000 with 50 bp single-end reads.

Identification of differentially expressed genes (DEGs) in ovarian stroma

Clean reads were mapped to the black rockfish reference genome (PRJNA516036) using STAR v.2.7.11b (Dobin et al., 2013), and transcripts were quantified with StringTie v.3.0.0 (Pertea et al., 2015). Unique mapped reads and TPM values (Transcripts Per Million) were retrieved, and DEGs were identified using DESeq2 (adjusted $P<0.05$, $|\log_2(\text{fold change})|>1$) (Love et al., 2014). Functional enrichment of DEGs was assessed with clusterProfiler (v.4.4.4) for GO and KEGG (FDR<0.05). Stage-specific expression modules were inferred by Mfuzz (v.2.69.0), and protein-protein interaction (PPI) networks were analyzed with STRING and visualized in Cytoscape v3.10.1.

Identification of differentially expressed exosomal miRNAs, lncRNAs, and mRNAs (DEMs, DELs, DEGs)

Clean reads were mapped to the black rockfish reference genome using Bowtie v1.3.1 and annotated against Rfam v.15.0, cDNA sequences, and repeat elements. Unmapped reads were aligned to human and zebrafish miRNA datasets (miRBase v22.1), and exosomal miRNAs were identified using miRDeep2 v.2.0.1.2 (Friedländer et al., 2008). miRNA abundance was normalized as RPM, low-abundance miRNAs (average<1 RPM) were excluded, and differentially expressed miRNAs (DEMs) were identified using DESeq2 (adjusted $P<0.05$, |log2(fold change)|>1). Transcript assembly was performed with StringTie v.3.0.0, and

candidate lncRNAs (>200 nt, >1 exon, class codes i/j/o/u/x) were screened for coding potential using TransDecoder, CPAT, CPC2, PLEK, and CNCI, with sequences showing Pfam or nr hits removed. Expression levels were quantified with Salmon v.1.10.3, and differentially expressed lncRNAs (DELs) and known protein coding transcripts (DETs) were identified using DESeq2. miRNA target genes were predicted using miRanda, TargetScan, RNAhybrid, and TargetFinder, and overlapping targets were retained for functional enrichment analysis. Cis- and trans-targets of lncRNAs were defined based on genomic proximity (within 100 kb) and Riblast prediction, respectively. Temporal expression patterns were analyzed using Mfuzz. Potential ceRNA interactions among miRNAs, lncRNAs, and mRNAs were inferred based on shared miRNA-binding sites and significant co-expression (Pearson's correlation, $|R|>0.7$, $P<0.05$), and the resulting networks were visualized using Cytoscape.

Proteomics analysis of exosomal protein

Proteomic quantification was performed by Novegene (China). Total proteins were extracted, digested with trypsin, desalted, and analyzed by LC-MS/MS using a data-independent acquisition (DIA) strategy. Raw data were processed with DIA-NN for peptide/protein identification and quantification. Functional annotation was conducted with GO, KEGG, and COG databases, and differentially expressed exosomal proteins (DEPs) were subsequently identified. Enrichment, temporal expression, and PPI analyses were performed as in the transcriptomic workflow.

Quantification RT-PCR (RT-qPCR)

cDNA was synthesized from ovarian tissue total RNA using the HiScript II Q RT SuperMix

for qPCR with gDNA Eraser (Vazyme, China), from ov-exos RNA using the miRNA 1st Strand cDNA Synthesis Kit (by tailing A, Vazyme, China), and from lncRNA using the HiScript IV All-in-One Ultra RT SuperMix for qPCR (Vazyme, China). 18S rRNA (KF430619.1) and U6 snRNA served as internal references. RT-qPCR was performed on a StepOne Plus™ Real-Time PCR System (Applied Biosystems, USA) with Taq Pro Universal SYBR qPCR Master Mix (High ROX, Vazyme, China). Relative expression levels were calculated using the $2^{-\Delta\Delta CT}$ method with three replicates. Primer sequences are provided in Supplementary Table S1.

Dual-luciferase reporter assays

The wild-type and mutant 3'-UTR of *hgfb* and lnc12398.1 were cloned into the pmiRGLO vector and co-transfected with miR-93-3p mimics or minics NC into 293 T cells. After 48h, luciferase activity was quantified using the Promega Dual-Luciferase Reporter Assay System. Each assay was independently repeated three times (Dualucif® Firefly & Renilla Assay Kit, UElandy, China).

Statistical analysis

All data are presented as the mean±standard error of the mean, and measurements were carried out in triplicates. All statistical procedures and graphs were generated using GraphPad Prism 9. Significance between two or more groups was analysed using Student's t-test or one-way ANOVA. One-way ANOVA was performed, followed by Tukey-HSD multiple range tests. P <0.05 were considered statistically significant. Correlation coefficients were computed using Pearson's algorithm.

RESULTS

Morphological and transcriptomic characteristics of the maternal component of the placental analogue

We first sought to elucidate the morphological features associated with the fine-scale construction of this transient organ and observed that, following fertilization, the original follicle layer enclosing the oocyte undergoes extensive remodeling to form a sac-like trophic structure surrounding the embryo (Figure 1A–C). This transformation is accompanied by robust proliferation and invasion of the ovarian stromal vasculature and extensive folding and elongation of the follicular tissue, greatly expanding the maternal-embryo interface. The outer follicle layer, composed of connective tissue, was highly vascularized, showing a 1.5-fold increase in capillary branching density and a 1.2-fold increase in average branch length compared to the vitellogenic stage (Figure 1D). Apoptosis of the inner follicle layer occurred in early gestation (Figure 2B), whereas by mid-gestation a newly formed follicular epithelium had developed, characterized by apical elongate microvilli and surface invaginations (Figure 2A). The follicular epithelium contains abundant endosomal vesicles, smooth endoplasmic reticulum, mitochondria, and Golgi complex, indicative of strong capacities for nutrient synthesis, transport, and steroidogenesis. The presence of numerous apical vesicles suggests active absorption and processing of follicular fluid. Capillaries are embedded in the basal portion of the follicular epithelium, with endothelial cells exhibiting numerous transcytotic vesicles (Figure 2C, D). Macrophages adjacent to the follicle layer, together with lymphocytes, were observed in the ovarian stroma (Figure 2E, F), suggesting a role in tissue remodeling and

immunoregulation.

To capture dynamic molecular changes associated with the transition of ovarian tissue into a functional placenta during gestation, transcriptomic analysis of twelve cDNA libraries identified 1 501 DEGs (Supplementary Figure S2; Supplementary table S2). Temporal trajectory analysis identified 590 continuously upregulated and 243 downregulated DEGs (Supplementary table S3), enriched in activation of immune cell, mesenchymal-epithelial transition (MET), and angiogenesis (Figure 3A–D), suggesting integrated physiological mechanisms driving placental analogue formation (Supplementary Figure S3). Functional associations were analyzed via STRING-based PPI networks, and several hub DEGs were validated by qRT-PCR (Figure 3E). In the functional networks, numerous genes potentially contributing to different aspects of placental analogue development were further identified, including *kdrl*, *egfl7*, *fgf1a*, *sema3e*, and *plxnd1* (angiogenesis); *mmp14*, *fn1a*, *mgp*, *tgfbr2b* and *bmp16* (tissue remodeling); *itgb8*, *cx43*, and *itga6* (cell junctions); and *il1b*, *csf1rb*, and *tnfsf14* (immune response) (Supplementary Figure S4). Importantly, many upregulated DEGs correspond to genes highly expressed in the human placenta, highlighting evolutionary convergence in placental development (Supplementary Figure S5)

Potential role of ov-exos in the formation of placental analogue

Notably, exosomes were observed within the placental analogue, particularly on the apical surface and proximate to the microvilli of the follicular epithelium (Figure 2C, right panel; Figure 2F). During gestation, the ovary exhibited significant upregulation of exosome-associated genes, including *cd63*, *cd9*, *cd81*, *alix*, *chmp4b*, *smpd3*, and *rab27b* mRNAs, as well

as Cd63, Cd9, and Tsg101 proteins, three well-established exosomal markers selected based on the cross-species reactivity of the antibodies used (Figure 4A, B), indicating enhanced exosome secretion. In addition, ISH and IHC revealed that Cd63 positive signals were primarily detected in the embryo, as well as in the ovarian stroma and follicle layer (Figure 4C, D), indicating that both maternal and fetal tissues contribute to exosome production and suggesting the possibility of bidirectional communication between mother and fetus. To assess the functional contribution of exosomes to placental analogue formation, ov-exos were isolated by ultracentrifugation and were confirmed by the presence of positive exosome markers (Cd63, Cd9, and Tsg101). Morphological and particle size characterization by TEM and DLS revealed that ov-exos exhibited the typical cup-shaped appearance with an average particle diameter ranging from 50 to 200 nanometers (Figure 4E–G).

Stage-specific expression profiling of exosomal cargo

Proteomics and transcriptomics were used to analyze the dynamic changes of exosomal cargos across developmental stages corresponding to the ovarian stromal transcriptome. A total of 7 127 exosomal proteins were identified in proteome (Figure 5A–E), many associated with epithelial cell junctions and microvilli formation (Supplementary Figure S6), predominantly of cytoplasmic or membrane origin (Supplementary Table S4). Of these, 1 772 were differentially expressed across different gestation stage (Figure 6F; Supplementary Table S5), enriched in epithelial tissue development, cytoskeleton reassembly, cell junction complex, epithelial cell polarization, nutrient synthesis and transport, energetic metabolism, and immunoregulation (Figure 5G, H). For RNA cargos, stage-specific exosomal smallRNA profiling uncovered 415

miRNAs (328 known and 87 novel miRNAs; Supplementary Fig. S7; Supplementary Table S6), with 214 differentially expressed and temporal analysis identifying continuously 90 upregulated and 43 downregulated miRNAs (Figure 6A; Supplementary Table S7), whose predicted targets were enriched in pathways related to tissue remodeling, protein processing, signal transmission, nutrient transport, metabolism, immune response, and post-transcriptional regulation (Figure 6B–D). Moreover, strand-specific lncRNA-seq identified 503 exosomal lncRNAs and 2 072 exosomal mRNAs with dynamic expression across gestation (Supplementary Figures S8; Supplementary Tables S8, S9). Within the set of DELs, 67 showed sustained upregulation and 57 sustained downregulation (Figure 6E), regulating protein synthesis and processing, blood vascular sprouting, cell fate determination, nutrient transport, and intracellular signaling transduction (Figure 6F–G). Similarly, the continuously up- and downregulated DETs exhibited comparable functional roles (Supplementary Figures S9; Supplementary Table S10).

Integration of exosomal ceRNA network with ovarian stroma DEGs

To investigate the interactions among exosomal cargos, an exosomal ceRNA network comprising 43 DELs, 71 DEMs, and 1 040 DETs was constructed, including 288 lncRNA-miRNA and 11,847 miRNA-mRNA pairs (Figure 7A; Supplementary Table S11), and functional analysis revealed that the DETs were involved in immune response, MET, and angiogenesis (Figure 7B–D). Therefore, the differentially expressed functional RNAs and proteins delivered by exosomes may exert coordinated roles in biomacromolecule synthesis and transport, cytoskeleton organization, ECM remodeling, signal transduction and cell

communication (Supplementary Figure S10). Integrative analysis of ov-exos and ovarian stroma transcriptomes identified co-upregulated mRNAs, four of which (*edil3a*, *efna5b*, *hgfb*, and *ptn*) were also present in the ceRNA network and highlighted as potential key messengers of exosome-placental analogue interaction (Figure 8A, B). The expression levels of these four candidates were examined by RT-qPCR across different developmental stages in both ovarian stroma and ov-exos, with *hgfb* exhibiting the most significant upregulation (Figure 8C, D). In addition, the binding interactions between *hgfb* mRNA and its associated miRNA and lncRNA were experimentally validation (Supplementary Figure S11).

Ov-exos are internalized by primary ovarian cells to deliver functional molecules

RNase protection assays demonstrated that, except for *ptn*, other transcripts resisted RNase I digestion, indicating that they are encapsulated within ov-exos (Figure 9A). We investigated whether *hgfb* transcripts could be transferred to primary ovarian cells via ov-exos. Fluorescence microscopy visualized the uptake of Exo-Tracker-labeled ov-exos (Magenta) into the cytoplasm of cells, and the abundance of *hgfb* transcripts was significantly increased (Figure 9B, C). Furthermore, DISH analysis revealed co-localization of *hgfb* transcripts with endothelial cells marked by *pecam1*, a vascular endothelial marker, and with *plxnd1*, an angiogenesis-related DEG identified from the ovarian stromal transcriptome, within blood vessels of the follicular layer and interstitial tissues (Figure 9D). HGF typically functions via autocrine or paracrine signaling, and immunofluorescence colocalization experiments further suggest that Hgfb exerts its effects on vascular endothelial cells via its cognate receptor, cMet (Figure 9E). Stimulation of ex vivo cultured ovarian microvascular endothelial cells with

recombinant Hgfb protein led to a significant upregulation of angiogenesis-related marker genes (Figure 9F; Supplementary Figure S12), supporting a functional role for Hgfb in vascular development. Together, these results suggest that ov-exos act as carriers of bioactive molecules, delivering of regulatory bioactive molecules to vascular endothelial cells and influencing cellular phenotype and transcriptional programs (Figure 9G).

DISCUSSION

Our comparative morphological analysis revealed that the black rockfish placental analogue, an interface structure located at the maternal-fetal boundary, derived from the ovarian follicle, is highly vascularized and extensively folded into large lamellae that envelop the fetus. Compared with the previously existing follicular layers, the post-fertilization placental tissues become thinner and provide a larger exchange surface, likely enhancing nutrient transfer efficiency. Moreover, this study provides the first description of the ultrastructure of the maternal component of the black rockfish placental analogue. The original follicular wall undergoes profound structural remodeling, marked by rupture of the inner follicular layer and the development of a microvillous follicular epithelium that becomes both glandular and endocrinologically active. Such features resemble those reported for the follicular placenta of poeciliid and anableps fishes (Grove & Wourms, 1991; Jollie & Jollie, 1964; Knight et al., 1985). The abundant transport vesicles and phagosomes suggest that the follicular epithelium may secrete protein, lipids into the follicular fluid (Veith, 1979), while also absorbing the fluid to process fetal respiratory and metabolic byproducts, as well as extracellular bioactive molecules. Morphologically and functionally, this newly formed follicular epithelium parallels

413 the chorionic trophoblast (Yabe et al., 2016), functioning as the maternal-fetal interface and
414 undergoing adaptive responses to local signals that support pregnancy.
415 Compared with the pre-fertilization stage, the ovarian stroma of gestational black rockfish
416 displayed a pronounced upregulation of DEGs associated with placental development,
417 particularly those governing tissue morphogenesis, including angiogenesis, MET, cell adhesion
418 and junctional complexes, and ECM remodeling, a subset of which are evolutionarily
419 conserved and likewise expressed in the human placenta. In decidualization, MET drives the
420 generation of an epithelioid phenotype (Pei et al., 2019; Zhang et al., 2013). Cell adhesion
421 molecules and junction proteins are upregulated, mediating intercellular interactions that
422 regulate paracellular permeability and maintain epithelial apical-basal polarity (Schumann et
423 al., 2015; Wang et al., 2004; Zhang et al., 2012). While a uterine myometrium-like structure
424 has not been identified in viviparous teleost, the establishment of the maternal-fetal interface
425 nevertheless depends on the coordinated interactions between cell adhesion molecules and
426 components of the ECM, as shown in the follicular epithelium of *Heterandria formosa* (Grove
427 & Wourms, 1994). In parallel with the formation of follicular epithelium characterized by
428 strong biosynthetic and transport capacities, the upregulation of genes associated with vascular
429 development suggests that the expanded and proliferating vasculature may enhance nutrient
430 supply to the developing embryo. Moreover, our results suggest that, during gestation,
431 immune-related cells, including macrophages, undergo substantial gene expression
432 reprogramming and may play key roles in maintaining the gestational environment and
433 mediating tissue remodeling (Lash et al., 2016; Parasar et al., 2021; Sun et al., 2021).

Active maternal-fetal crosstalk contributes positively to placental formation. However, unlike mammalian placentation, the maternal and fetal compartments in black rockfish are separated by a dense eosinophilic fluid, which hinders the exchange of signaling molecules between them (Wang et al., 2022), whereas exosomes, as extracellular nanovesicles with strong barrier-traversing capacity, enable communication across this otherwise restrictive interface (Witwer et al., 2019). We observed elevated exosome production in the gestational black rockfish ovary, with their distribution concentrated around the placental analogue, consistent with their recognized importance in placentation (Nakahara et al., 2020). Although directional exosome transport remains elusive due to Cd63 signals in both maternal and fetal tissues, gestation nonetheless requires bidirectional communication mediated by exosomes from both compartments (Czernek & Düchler, 2020). We demonstrated that ov-exos carry cell junction, cytoskeletal, and endometrial transport-related proteins, which are commonly presented in mammalian placental exosomes (Atay et al., 2011a; Ouyang et al., 2016). Membrane proteins enable cell recognition and internalization, while cell adhesion molecules govern intercellular and cell-ECM interactions (Lin et al., 2023; Xu et al., 2024). Among them, Integrins, a protein family enriched in ov-exos, are known key factors in placental formation (Baig et al., 2014; Segura-Benítez et al., 2022). Prior to embryo implantation, uterine epithelial cells undergo microvillar loss or shortening (Dudley et al., 2018; Murphy, 2000). Conversely, the follicular wall of gestational black rockfish exhibits elongated, densely packed microvilli, potentially under the regulation of Ezrin in ov-exos, a protein concentrated at the apical membrane of human placental syncytiotrophoblasts that contributes to microvilli assembly (Berryman et al.,

1993; Higuchi et al., 2010). Ezrin is likewise detected in syncytiotrophoblast-derived microvesicles (Baig et al., 2014), implicating it as a potential placental morphogenetic factor in black rockfish.

Exosomes precisely orchestrate maternal-fetal crosstalk and placental formation via their RNA cargo (Burkova et al., 2021; Maligianni et al., 2022). During early gestation, miR-451 (Li et al., 2015), miR-181a (Su et al., 2014), and miR-499-5p (Zhao et al., 2018) are involved in embryonic implantation, consistent with their post-fertilization upregulation in ov-exos. Although certain exosomal miRNAs are known to mediate trophoblast-endometrium interactions (Das & Kale, 2020), most showed no significant differences in our study, suggesting that selective exosomal packaging and miRNA-target RNA interactions underlie context-dependent functional divergence (Kostyniuk & Mennigen, 2020). lncRNAs exhibit an additional epigenetic mechanism, acting as miRNA sponges within the ceRNA network, and play pivotal roles in gestation (Wang et al., 2023). The ceRNA network in ov-exos mirrored key functions of stromal DEGs, supporting a close association and context-dependent regulatory roles of exosomal ncRNAs in placental analogue development in black rockfish (Maligianni et al., 2022). However, we prioritized candidate mRNAs within the ceRNA network for functional validation, as they may increase the abundance of their corresponding mRNAs and the production of their encoded proteins in recipient cells (Bland et al., 2018; Wu et al., 2017). Among the ceRNA network, *hgfb* was chosen due to its concurrent upregulation in both exosomes and recipient cells. Given that we primarily focused on the direct regulatory effects of exosome-delivered mRNAs, we only validated the interaction among *hgfb*, miR-93-

476 3p, and lnc12398.1 within the ceRNA network. Functional characterization of non-coding
477 RNAs was beyond the scope of this study, and the underlying molecular mechanisms will be
478 investigated in future work.
479 HGF functions as both a mitogen and a morphogen, orchestrating mesenchymal-epithelial
480 interactions between granulosa and theca cells, and additionally serving as a potent angiogenic
481 factor (Bussolino et al., 1992; Parrott et al., 1994; Uzumcu et al., 2006). Following fertilization,
482 *hgfb* is upregulated in both ov-exos and the ovarian stroma, potentially facilitating the
483 transformation of the follicle into a placental analogue. HGF and its receptor c-Met are
484 localized to overlapping or separate compartments of the villous trophoblast, functioning via
485 autocrine and paracrine signaling to promote placentation (Clark et al., 1996; Kilby et al., 1996;
486 Y. Ma et al., 2021). In our study, ov-exos are internalized by ovarian cells, after which recipient
487 cells may produce and secrete more Hgfb, potentially functioning in a similar manner. Given
488 that angiogenesis is essential for placental development, DISH and IHC assays were then
489 employed to verify the delivery of *hgfb* mRNA to Cd31-positive vascular endothelial cells
490 within the placental analogue, with the resulting upregulation of angiogenic genes (*plxnd1*).
491 Given that black rockfish reproduces via internal fertilization, the precise developmental stage
492 cannot be accurately determined without ovarian dissection. It is currently not technically
493 feasible to obtain fertilized embryos at appropriate developmental stages for microinjection-
494 based genetic loss-of-function studies. Thus, we used recombinant protein to preliminarily
495 assess the pro-angiogenic function of Hgfb. Although our study was limited to the angiogenic
496 function of Hgfb, Hgfb/cMet signaling is known to elicit complex phenotypic responses

through receptor tyrosine kinase pathways-mediated downstream signaling networks, which may collectively coordinate ovarian tissue remodeling (Organ & Tsao, 2011).

Collectively, we delineated the morphological and transcriptional features of the black rockfish placental analogue and underscored the role of ov-exos, particularly the bioactive cargos they convey, in driving the transition of ovarian follicular tissue to a functional placental analogue. Given the difficulties in isolating pure tissue-derived exosomes (Li et al., 2019), we focused our attention to their RNA cargo, such as *hgfb*, raising the need for future studies to elucidate the molecular regulatory axis through which exosomes mediate ovarian tissue remodeling. Importantly, we emphasize the critical role of *hgfb* in normal gestation, as its significant downregulation in the ovarian stroma under abnormal gestation conditions was observed (Supplementary Figure S12). The pro-angiogenic activity of recombinant Hgfb protein further supports its role in driving the formation of the placental analogue, which is characterized primarily by vascular expansion. Furthermore, we plan to exploit exosomes as delivery vehicles for CRISPR components to the ovary to achieve *hgfb* loss-of-function, which will facilitate a better understanding of its role in reproductive adaptation. However, the cellular origin of ov-exos remains an open question, given that exosomes are released by almost all cell types; resolving this challenge is essential for clarifying the mechanisms underlying exosome-mediated maternal-fetal interaction. Overall, these findings not only deepen our understanding of the unique reproductive adaptations of viviparous teleost and offer a valuable case for studying the convergent evolution of vertebrate viviparity.

DATA AVAILABILITY

RNA sequencing data of ovarian stroma and ov-exos have been deposited at the NCBI Sequence Read Archive (SRA) under BioProjectID PRJNA1454908. SmallRNA sequencing data of ov-exos have been deposited at the NCBI SRA under BioProjectID PRJNA1455192.

SUPPLEMENTARY DATA

Supplementary data to this article can be found online.

COMPETING INTERESTS

The authors declare that they have no competing interests.

AUTHORS' CONTRIBUTIONS

Z.B.Y. carried out data analyses, interpreted findings, ensured data accuracy, assisted with data visualization, and prepared the initial manuscript draft. X.Q. conceived the study, acquired funding, provided overall supervision, ensured data integrity, critically revised the manuscript, and coordinated the research team. H.S.W., Y.L and L.K.L. suggested substantial revisions to improve clarity and coherence. X.J.W., J.S.L, and X.L.Y. were responsible for collecting and processing samples. All authors read and approved the final version of the manuscript.

ACKNOWLEDGMENTS

Thanks for the support provided by the Marine Biodiversity and Evolution Research Institute's Instrument and Equipment Sharing Platform, specifically the high-speed centrifuge (XPN-100).

References

Apostolov A, Mladenović D, Tilk K, et al. 2025. Multi-omics analysis of uterine fluid extracellular vesicles reveals a resemblance with endometrial tissue across the menstrual cycle: Biological and translational insights. *Human Reproduction Open*, **2025**(2): hoaf010. DOI: 10.1093/hropen/hoaf010.

Askenase PW. 2021. Ancient evolutionary origin and properties of universally produced natural exosomes contribute to their therapeutic superiority compared to artificial nanoparticles. *International journal of molecular sciences*, **22**(3): 1429. DOI: 10.3390/ijms22031429.

Atay S, Gercel-Taylor C, Kesimer M, et al. 2011a. Morphologic and proteomic characterization of exosomes released by cultured extravillous trophoblast cells. *Experimental Cell Research*, **317**(8): 1192–1202. DOI: 10.1016/j.yexcr.2011.01.014.

Atay S, Gercel-Taylor C, Suttles J, et al. 2011b. Trophoblast-derived exosomes mediate monocyte recruitment and differentiation: MONOCYTE EDUCATION BY TROPHOBLAST EXOSOMES. *American Journal of Reproductive Immunology*, **65**(1): 65–77. DOI: 10.1111/j.1600-0897.2010.00880.x.

Baig S, Kothandaraman N, Manikandan J, et al. 2014. Proteomic analysis of human placental syncytiotrophoblast microvesicles in preeclampsia. *Clinical Proteomics*, **11**(1): 40. DOI: 10.1186/1559-0275-11-40.

Berryman M, Franck Z, Bretscher A. 1993. Ezrin is concentrated in the apical microvilli of a wide variety of epithelial cells whereas moesin is found primarily in endothelial cells. *Journal of Cell Science*, **105**(4): 1025–1043. DOI: 10.1242/jcs.105.4.1025.

Blackburn DG. 2015. Evolution of vertebrate viviparity and specializations for fetal nutrition: A quantitative and qualitative analysis. *Journal of Morphology*, **276**(8): 961–990. DOI: 10.1002/jmor.20272.

Bland CL, Byrne-Hoffman CN, Fernandez A, et al. 2018. Exosomes derived from B16F0 melanoma cells alter the transcriptome of cytotoxic T cells that impacts mitochondrial respiration. *The FEBS journal*, **285**(6): 1033–1050. DOI: 10.1111/febs.14396.

Boehlert GW, Yoklavich MM. 1984. Reproduction, embryonic energetics, and the maternal-fetal relationship in the viviparous genus sebastes (pisces: Scorpaenidae). *Biological Bulletin*, **167**(2): 354–370. DOI: 10.2307/1541282.

Burkova EE, Sedykh SE, Nevinsky GA. 2021. Human placenta exosomes: Biogenesis, isolation, composition, and prospects for use in diagnostics. *International journal of molecular sciences*, **22**(4): 2158. DOI: 10.3390/ijms22042158.

Bussolino F, Di Renzo MF, Ziche M, et al. 1992. Hepatocyte growth factor is a potent angiogenic factor which stimulates endothelial cell motility and growth. *The Journal of Cell Biology*, **119**(3): 629–641. DOI: 10.1083/jcb.119.3.629.

Chen C, Zhang Z, Gu X, et al. 2023. Exosomes: new regulators of reproductive development. *Materials Today Bio*, **19**: 100608. DOI: 10.1016/j.mtbio.2023.100608.

Chen Y, Zhao X, Men Y, et al. 2024. Regulation of sperm motility by exosomes of ovarian fluid during female sperm storage in black rockfish (sebastes schlegelii). *Aquaculture*, **592**: 741189. DOI: 10.1016/j.aquaculture.2024.741189.

Clark DE, Salvig JD, Smith SK, et al. 1998. Hepatocyte growth factor levels during normal and intra-uterine growth-restricted pregnancies. *Placenta*, **19**(8): 671–673. DOI: 10.1016/S0143-4004(98)90029-7.

Clark DE, Smith SK, Sharkey AM, et al. 1996. Hepatocyte growth factor/scatter factor and its receptor c-met: Localisation and expression in the human placenta throughout

582 pregnancy. *The Journal of Endocrinology*, **151**(3): 459–467. DOI:
583 10.1677/joe.0.1510459.
584 Cross JC, Baczyk D, Dobric N, et al. 2003. Genes, Development and Evolution of the Placenta.
585 *Placenta*, **24**(2–3): 123–130. DOI: 10.1053/plac.2002.0887.
586 Czernek L, Düchler M. 2020. Exosomes as Messengers between Mother and Fetus in
587 Pregnancy. *International journal of molecular sciences*, **21**(12): 4264. DOI:
588 10.3390/ijms21124264.
589 Das M, Kale V. 2020. Extracellular vesicles: Mediators of embryo-maternal crosstalk during
590 pregnancy and a new weapon to fight against infertility. *European Journal of Cell*
591 *Biology*, **99**(8): 151125. DOI: 10.1016/j.ejcb.2020.151125.
592 Di Cesare L, Barbeito CG, Santamaría-Martín C, et al. 2023. Ovarian changes and development
593 of the branchial placenta occurring in jenynsia lineata (cyprinodontiformes,
594 anablepidae). *Journal of Morphology*, **284**(9): e21630. DOI: 10.1002/jmor.21630.
595 Diamant I, Clarke DJB, Evangelista JE, et al. 2025. Harmonizome 3.0: Integrated knowledge
596 about genes and proteins from diverse multi-omics resources. *Nucleic Acids Research*,
597 **53**(D1): D1016–D1028. DOI: 10.1093/nar/gkae1080.
598 Dobin A, Davis CA, Schlesinger F, et al. 2013. STAR: Ultrafast universal RNA-seq aligner.
599 *Bioinformatics*, **29**(1): 15–21. DOI: 10.1093/bioinformatics/bts635.
600 Dudley JS, Murphy CR, Thompson MB, et al. 2018. Uterine epithelial cells undergo a plasma
601 membrane transformation during early pregnancy in the domestic cat (<span
602 style="font-variant:Small-caps;"> *felis catus*). *Anatomical Record*, **301**(9):
603 1497–1505. DOI: 10.1002/ar.23895.
604 Fagerberg L, Hallström BM, Oksvold P, et al. 2014. Analysis of the human tissue-specific
605 expression by genome-wide integration of transcriptomics and antibody-based
606 proteomics. *Molecular & Cellular Proteomics*, **13**(2): 397–406. DOI:
607 10.1074/mcp.M113.035600.
608 Friedländer MR, Chen W, Adamidi C, et al. 2008. Discovering microRNAs from deep
609 sequencing data using miRDeep. *Nature Biotechnology*, **26**(4): 407–415. DOI:
610 10.1038/nbt1394.
611 Grove BD, Wourms JP. 1991. The follicular placenta of the viviparous fish, *heterandria*
612 *formosa* . I. Ultrastructure and development of the embryonic absorptive surface.
613 *Journal of Morphology*, **209**(3): 265–284. DOI: 10.1002/jmor.1052090304.
614 Grove BD, Wourms JP. 1994. Follicular placenta of the viviparous fish, *heterandria formosa* :
615 II. Ultrastructure and development of the follicular epithelium. *Journal of Morphology*,
616 **220**(2): 167–184. DOI: 10.1002/jmor.1052200206.
617 Guernsey MW, Van Kruistum H, Reznick DN, et al. 2020. Molecular signatures of placentation
618 and secretion uncovered in poeciliopsis maternal follicles. *Molecular Biology and*
619 *Evolution*, (J. Kelley, ed.)**37**(9): 2679–2690. DOI: 10.1093/molbev/msaa121.
620 He Y, Chang Y, Bao L, et al. 2019. A chromosome-level genome of black rockfish, *sebastes*
621 *schlegelii* , provides insights into the evolution of live birth. *Molecular Ecology*
622 *Resources*, **19**(5): 1309–1321. DOI: 10.1111/1755-0998.13034.

623 Higuchi K, Iizasa H, Sai Y, et al. 2010. Differential expression of ezrin and CLP36 in the two
624 layers of syncytiotrophoblast in rats. *Biological and Pharmaceutical Bulletin*, **33**(8):
625 1400–1406. DOI: 10.1248/bpb.33.1400.
626 Jollie WP, Jollie LG. 1964. The fine structure of the ovarian follicle of the ovoviviparous
627 poeciliid fish, *lebistes reticulatus* . I. Maturation of follicular epithelium. *Journal of*
628 *Morphology*, **114**(3): 479–501. DOI: 10.1002/jmor.1051140308.
629 Ju G, Cheng J, Zhong L, et al. 2015. Microvesicles derived from human umbilical cord
630 mesenchymal stem cells facilitate tubular epithelial cell dedifferentiation and growth
631 via hepatocyte growth factor induction. *PloS One*, **10**(3): e0121534. DOI:
632 10.1371/journal.pone.0121534.
633 Kilby MD, Afford S, Li XF, et al. 1996. Localisation of hepatocyte growth factor and its
634 receptor (c-met) protein and mRNA in human term placenta. *Growth Factors (Chur,*
635 *Switzerland)*, **13**(1–2): 133–139. DOI: 10.3109/08977199609034573.
636 Knight FM, Lombardi J, Wourms JP, et al. 1985. Follicular placenta and embryonic growth of
637 the viviparous four-eyed fish (*anableps*). *Journal of Morphology*, **185**(1): 131–142.
638 DOI: 10.1002/jmor.1051850110.
639 Kostyniuk DJ, Mennigen JA. 2020. Meta-analysis of differentially-regulated hepatic
640 microRNAs identifies candidate post-transcriptional regulation networks of
641 intermediary metabolism in rainbow trout. *Comparative Biochemistry and Physiology,*
642 *Part D: Genomics & Proteomics*, **36**: 100750. DOI: 10.1016/j.cbd.2020.100750.
643 Lash GE, Pitman H, Morgan HL, et al. 2016. Decidual macrophages: key regulators of vascular
644 remodeling in human pregnancy. *Journal of Leukocyte Biology*, **100**(2): 315–325. DOI:
645 10.1189/jlb.1A0815-351R.
646 Li X, Corbett AL, Taatizadeh E, et al. 2019. Challenges and opportunities in exosome research-
647 perspectives from biology, engineering, and cancer therapy. *APL Bioengineering*, **3**(1):
648 011503. DOI: 10.1063/1.5087122.
649 Li Z, Jia J, Gou J, et al. 2015. MicroRNA-451 plays a role in murine embryo implantation
650 through targeting Ankrd46, as implicated by a microarray-based analysis. *Fertility and*
651 *Sterility*, **103**(3): 834-844.e4. DOI: 10.1016/j.fertnstert.2014.11.024.
652 Lin W, Fang J, Wei S, et al. 2023. Extracellular vesicle-cell adhesion molecules in tumours:
653 Biofunctions and clinical applications. *Cell Communication and Signaling: CCS*, **21**(1):
654 246. DOI: 10.1186/s12964-023-01236-8.
655 Lombardi J, Wourms JP. 1985. The trophotaenial placenta of a viviparous goodeid fish. I.
656 Ultrastructure of the internal ovarian epithelium, the maternal component. *Journal of*
657 *Morphology*, **184**(3): 277–292. DOI: 10.1002/jmor.1051840304.
658 Love MI, Huber W, Anders S. 2014. Moderated estimation of fold change and dispersion for
659 RNA-seq data with DESeq2. *Genome Biology*, **15**(12): 550. DOI: 10.1186/s13059-014-
660 0550-8.
661 Lyu L, Wang R, Wen H, et al. 2022. Cyclooxygenases of ovoviviparous black rockfish
662 (sebastes schlegelii): Cloning, tissue distribution and potential role in mating and
663 parturition. *Comparative Biochemistry and Physiology Part B: Biochemistry and*
664 *Molecular Biology*, **257**: 110677. DOI: 10.1016/j.cbpb.2021.110677.

Lyu L, Yao Y, Xie S, et al. 2024. Mating behaviors in ovoviviparous black rockfish (sebastes schlegelii): Molecular function of prostaglandin E2 as both a hormone and pheromone. *Marine Life Science & Technology*, **6**(1): 15–30. DOI: 10.1007/s42995-023-00214-w.

Ma Q, Beal JR, Bhurke A, et al. 2022. Extracellular vesicles secreted by human uterine stromal cells regulate decidualization, angiogenesis, and trophoblast differentiation. *Proceedings of the National Academy of Sciences*, **119**(38): e2200252119. DOI: 10.1073/pnas.2200252119.

Ma R, Liang Z, Shi X, et al. 2021. Exosomal miR-486-5p derived from human placental microvascular endothelial cells regulates proliferation and invasion of trophoblasts via targeting IGF1. *Human Cell*, **34**(5): 1310–1323. DOI: 10.1007/s13577-021-00543-x.

Ma Y, Yu X, Li Y-X, et al. 2021. HGF/c-met signaling regulates early differentiation of placental trophoblast cells. *The Journal of Reproduction and Development*, **67**(2): 89–97. DOI: 10.1262/jrd.2020-107.

Maligianni I, Yapijakis C, Nousia K, et al. 2022. Exosomes and exosomal non-coding RNAs throughout human gestation (review). *Experimental and Therapeutic Medicine*, **24**(3): 582. DOI: 10.3892/etm.2022.11518.

Mori H, Nakagawa M, Soyano K, et al. 2003. Annual reproductive cycle of black rockfish sebastes schlegeli in captivity. *Fisheries Science*, **69**(5): 910–923. DOI: 10.1046/j.1444-2906.2003.00707.x.

Murphy CR. 2000. The plasma membrane transformation of uterine epithelial cells during pregnancy. *Journal of Reproduction and Fertility. Supplement*, **55**: 23–28.

Nakahara A, Nair S, Ormazabal V, et al. 2020. Circulating placental extracellular vesicles and their potential roles during pregnancy. *Ochsner Journal*, **20**(4): 439–445. DOI: 10.31486/toj.20.0049.

Olivera-Tlahuel C, Moreno-Mendoza NA, Villagrán-Santa Cruz M, et al. 2019. Placental structures and their association with matrotrophy and superfetation in poeciliid fishes. *Acta Zoologica*, **100**(2): 167–181. DOI: 10.1111/azo.12244.

Organ SL, Tsao M-S. 2011. An overview of the c-MET signaling pathway. *Therapeutic Advances in Medical Oncology*, **3**(1_suppl): S7–S19. DOI: 10.1177/1758834011422556.

Ouyang Y, Bayer A, Chu T, et al. 2016. Isolation of human trophoblastic extracellular vesicles and characterization of their cargo and antiviral activity. *Placenta*, **47**: 86–95. DOI: 10.1016/j.placenta.2016.09.008.

Pan Y, Meng L, Yoshida K, et al. 2025. Comparative and functional analysis of exosomal microRNAs during semelparous reproduction in ayu fish (*plecoglossus altivelis*). *Journal of Extracellular Biology*, **4**(3): e70038. DOI: 10.1002/jex2.70038.

Parasar P, Guru N, Nayak NR. 2021. Contribution of macrophages to fetomaternal immunological tolerance. *Human Immunology*, **82**(5): 325–331. DOI: 10.1016/j.humimm.2021.02.013.

Parrott JA, Vigne JL, Chu BZ, et al. 1994. Mesenchymal-epithelial interactions in the ovarian follicle involve keratinocyte and hepatocyte growth factor production by thecal cells

and their action on granulosa cells. *Endocrinology*, **135**(2): 569–575. DOI: 10.1210/endo.135.2.8033804.
Pei D, Shu X, Gassama-Diagne A, et al. 2019. Mesenchymal–epithelial transition in development and reprogramming. *Nature Cell Biology*, **21**(1): 44–53. DOI: 10.1038/s41556-018-0195-z.
Pertea M, Pertea GM, Antonescu CM, et al. 2015. StringTie enables improved reconstruction of a transcriptome from RNA-seq reads. *Nature Biotechnology*, **33**(3): 290–295. DOI: 10.1038/nbt.3122.
Rouillard AD, Gundersen GW, Fernandez NF, et al. 2016. The harmonizome: A collection of processed datasets gathered to serve and mine knowledge about genes and proteins. *Database*, **2016**: baw100. DOI: 10.1093/database/baw100.
Schindler JF, Hamlett WC. 1993. Maternal–embryonic relations in viviparous teleosts. *Journal of Experimental Zoology*, **266**(5): 378–393. DOI: 10.1002/jez.1402660506.
Schumann S, Buck VU, Classen-Linke I, et al. 2015. Claudin-3, claudin-7, and claudin-10 show different distribution patterns during decidualization and trophoblast invasion in mouse and human. *Histochemistry and Cell Biology*, **144**(6): 571–585. DOI: 10.1007/s00418-015-1361-z.
Segura-Benítez M, Carbajo-García MC, Corachán A, et al. 2022. Proteomic analysis of extracellular vesicles secreted by primary human epithelial endometrial cells reveals key proteins related to embryo implantation. *Reproductive Biology and Endocrinology*, **20**(1): 3. DOI: 10.1186/s12958-021-00879-x.
Su L, Liu R, Cheng W, et al. 2014. Expression patterns of MicroRNAs in porcine endometrium and their potential roles in embryo implantation and placentation. *PLoS ONE*, (X. Ye, ed.)**9**(2): e87867. DOI: 10.1371/journal.pone.0087867.
Sun F, Wang S, Du M. 2021. Functional regulation of decidual macrophages during pregnancy. *Journal of Reproductive Immunology*, **143**: 103264. DOI: 10.1016/j.jri.2020.103264.
Susaki EA, Tainaka K, Perrin D, et al. 2014. Whole-brain imaging with single-cell resolution using chemical cocktails and computational analysis. *Cell*, **157**(3): 726–739. DOI: 10.1016/j.cell.2014.03.042.
Tengfei D, Yongshuang X, Haixia Z, et al. 2021. Multiple fetal nutritional patterns before parturition in viviparous fish sebastes schlegelii (hilgendorf, 1880). *Frontiers in Marine Science*, **7**: 571946. DOI: 10.3389/fmars.2020.571946.
Uhlén M, Fagerberg L, Hallström BM, et al. 2015. Tissue-based map of the human proteome. *Science*, **347**(6220): 1260419. DOI: 10.1126/science.1260419.
Uzumcu M, Pan Z, Chu Y, et al. 2006. Immunolocalization of the hepatocyte growth factor (HGF) system in the rat ovary and the anti-apoptotic effect of HGF in rat ovarian granulosa cells in vitro. *Reproduction*, **132**(2): 291–299. DOI: 10.1530/rep.1.00989.
Van Kruistum H, Nijland R, Reznick DN, et al. 2021. Parallel Genomic Changes Drive Repeated Evolution of Placentas in Live-Bearing Fish. *Molecular Biology and Evolution*, (E. Teeling, ed.)**38**(6): 2627–2638. DOI: 10.1093/molbev/msab057.

746 Veith WJ. 1979. The chemical composition of the follicular fluid of the viviparous teleost
747 clinus superciliosus. *Comparative Biochemistry and Physiology Part A: Physiology*,
748 **63**(1): 37–40. DOI: 10.1016/0300-9629(79)90624-8.
749 Wang M, Zheng L, Ma S, et al. 2023. Biogenesis and function of exosome lncRNAs and their
750 role in female pathological pregnancy. *Frontiers in endocrinology*, **14**: 1191721. DOI:
751 10.3389/fendo.2023.1191721.
752 Wang X, Matsumoto H, Zhao X, et al. 2004. Embryonic signals direct the formation of tight
753 junctional permeability barrier in the decidualizing stroma during embryo implantation.
754 *Journal of Cell Science*, **117**(Pt 1): 53–62. DOI: 10.1242/jcs.00826.
755 Wang X, Meng W, Qi X, et al. 2022. Molecular characterization and expression patterns of
756 glucocorticoid receptors in the viviparous black rockfish sebastes schlegelii. *General*
757 *and Comparative Endocrinology*, **316**: 113947. DOI: 10.1016/j.ygcen.2021.113947.
758 Wang X, Wen H, Li Y, et al. 2021. Characterization of CYP11A1 and its potential role in sex
759 asynchronous gonadal development of viviparous black rockfish Sebastes schlegelii
760 (Sebastidae). *General and Comparative Endocrinology*, **302**: 113689. DOI:
761 10.1016/j.ygcen.2020.113689.
762 Witwer KW, Van Balkom BWM, Bruno S, et al. 2019. Defining mesenchymal stromal cell
763 (MSC)-derived small extracellular vesicles for therapeutic applications. *Journal of*
764 *Extracellular Vesicles*, **8**(1): 1609206. DOI: 10.1080/20013078.2019.1609206.
765 Wourms JP. 1981. Viviparity: The maternal-fetal relationship in fishes. *American Zoologist*,
766 **21**(2): 473–515. DOI: 10.1093/icb/21.2.473.
767 Wourms JP. 1991. Reproduction and development of sebastes in the context of the evolution
768 of piscine viviparity. *Rockfishes of the Genus Sebastes: Their Reproduction and Early*
769 *Life History*, G. W. Boehlert and J. Yamada, eds.111–126.
770 Wourms JP, Grove BD, Lombardi J. 1988. 1 the maternal-embryonic relationship in viviparous
771 fishes. *Fish Physiology*, 1–134.
772 Wu Y, Deng W, McGinley EC, et al. 2017. Melanoma exosomes deliver a complex biological
773 payload that upregulates PTPN11 to suppress T lymphocyte function. *Pigment Cell &*
774 *Melanoma Research*, **30**(2): 203–218. DOI: 10.1111/pcmr.12564.
775 Xu F, Luo S, Lu P, et al. 2024. Composition, functions, and applications of exosomal
776 membrane proteins. *Frontiers in Immunology*, **15**: 1408415. DOI:
777 10.3389/fimmu.2024.1408415.
778 Xu X, Wang X, Liu Q, et al. 2022. New insights on folliculogenesis and follicular placentation
779 in marine viviparous fish black rockfish (sebastes schlegelii). *Gene*, **827**: 146444. DOI:
780 10.1016/j.gene.2022.146444.
781 Yabe S, Alexenko AP, Amita M, et al. 2016. Comparison of syncytiotrophoblast generated
782 from human embryonic stem cells and from term placentas. *Proceedings of the National*
783 *Academy of Sciences*, **113**(19): . DOI: 10.1073/pnas.1601630113.
784 Zhang Ling, Patterson AL, Zhang Lihua, et al. 2012. Endometrial stromal beta-catenin is
785 required for steroid-dependent mesenchymal-epithelial cross talk and decidualization.
786 *Reproductive Biology and Endocrinology: RB&E*, **10**: 75. DOI: 10.1186/1477-7827-
787 10-75.

788 Zhang X-H, Liang X, Liang X-H, et al. 2013. The mesenchymal-epithelial transition during in
789 vitro decidualization. *Reproductive Sciences (thousand Oaks, Calif.)*, **20**(4): 354–360.
790 DOI: 10.1177/1933719112472738.
791 Zhao G, Yang C, Yang J, et al. 2018. Placental exosome-mediated bta-miR-499-Lin28B/let-7
792 axis regulates inflammatory bias during early pregnancy. *Cell Death and Disease*, **9**(6):
793 704. DOI: 10.1038/s41419-018-0713-8.

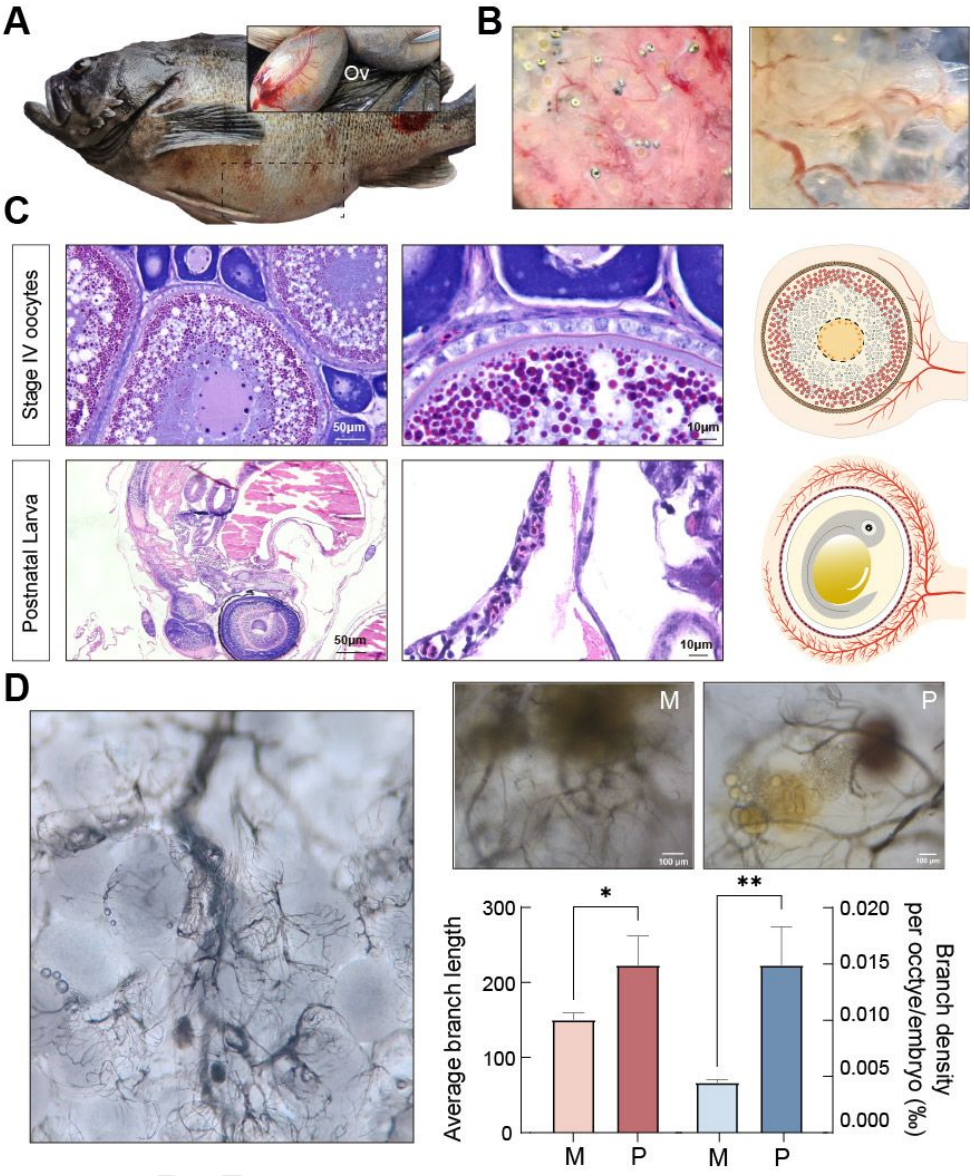

Figure 1. Morphological observation of the placental analogue of black rockfish

A–B: Photographs of black rockfish ovary and follicular tissue. C: Histomicrographs and a schematic diagram depicting Stage IV oocytes and pre-hatching embryos with their surrounding follicle layer. D: Analysis of the intrafollicular vasculature via India ink-gelatin perfusion. Overview (left) and magnification detailed (top right) view of the perfused capillaries enveloping Stage IV oocytes (mature stage, M) and pre-hatching embryos (P). Quantitative analysis of intrafollicular vasculature (bottom right). The average branch length and average branch point density were measured from three

random fields of view per stage. Statistical analysis was conducted using unpaired t-test. Error bars indicate standard error of the mean (SEM). *: $P<0.05$, **: $P<0.01$. Scale bars: 100 μm (D), 50 μm (C, left panel), 10 μm (C, middle panel).

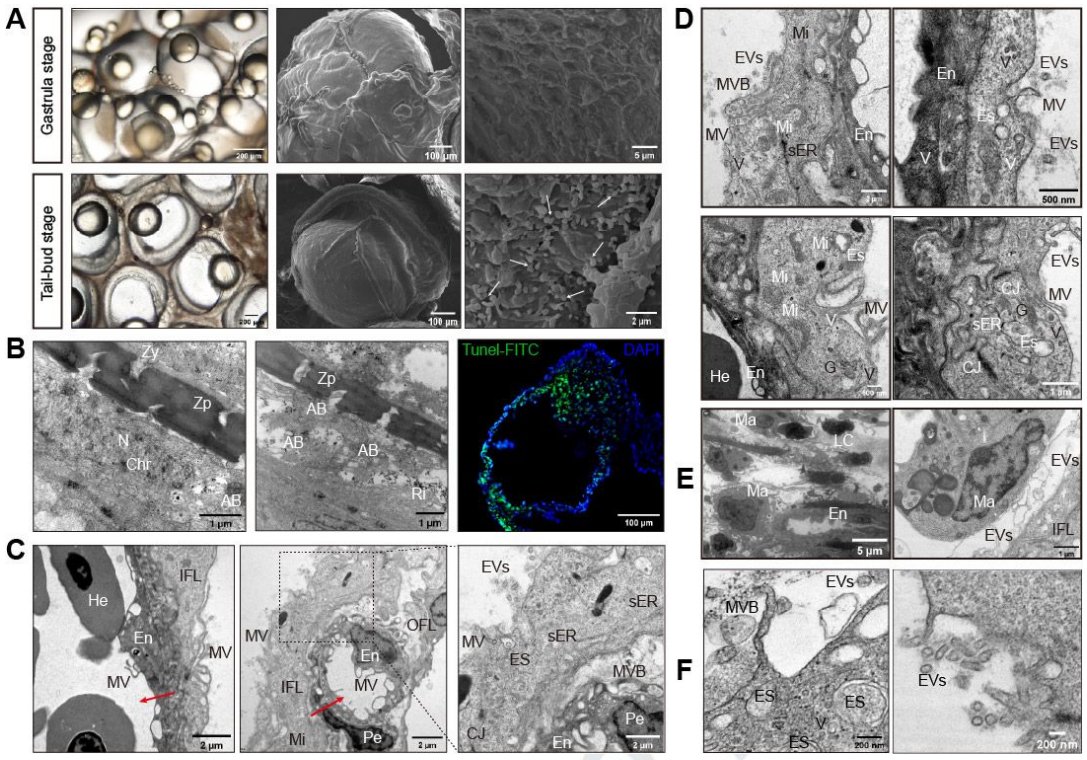

Figure 2. Ultrastructural characteristics of the placental analogue of black rockfish A: Optical and scanning electron micrographs showing the oocyte/embryo (left and middle) and the inner surface of the follicle layer (right), with microvilli indicated by white arrowheads. B: The granulosa cell undergoing apoptosis. Transmission electron micrographs showing reduced cell volume, detachment from neighboring cells, chromatin condensation, fragmentation of the nuclear envelope and nucleolus, followed by the formation of apoptotic bodies (AB) (left and middle). TUNEL assay showing positive apoptotic signal located in the inner follicle layer (right). C: Electron micrographs of placental analogues. The outer follicle layer (OFL) consists of connective tissue, with capillaries embedded in the ECM immediately beneath the follicular epithelium (indicated by red arrowheads), while the inner layer consists of follicular epithelium with active transport and endocrine functions. D: Section of the

inner follicle layer (IFL). A large number of microvilli (MV) are evident, along with subcellular structures related to nutrient secretion, steroidogenesis, and transport. E: Immune cells in the ovarian stroma (left panel). Macrophages are located adjacent to the inner follicle layer (right panel). F: Exosomes are present in the placental analogue. Zy, zygote; N, nucleus; Zp, Zona pellucida; Chr, chromosome; Ri, ribosome; He, hemocyte; En, endothelial cell; PE, pericyte; MVB, multivesicular body; V, vesicle; sER, smooth endoplasmic reticulum; G, Golgi apparatus; CJ, cell junctions; ES, endosome; Mi, mitochondrion; Ly, lymphocyte; Ma, macrophage. Scale bars: 200 μm (A, left), 100 μm (A, middle; B, right), 5 μm (A, top right; E, left), 2 μm (A, bottom right; C; D, top left), 1 μm (B, left and middle; D, bottom right; E, right), 500 nm (D, top right and bottom left), 200 nm (F).

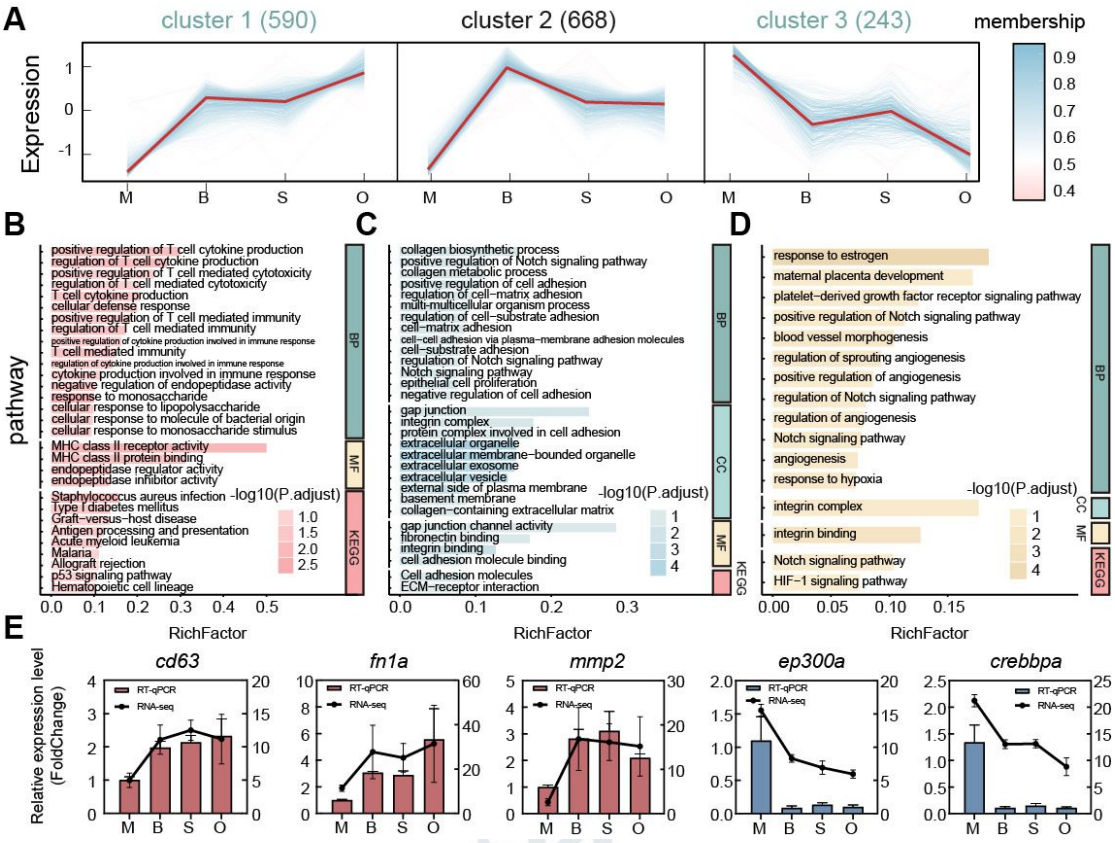

Figure 3. Temporal profiles and functional enrichment of DEGs in ovarian stroma

A: Mfuzz clustering analysis of DEGs identified three clusters with distinct temporal trends. Enrichment of continuously up- or down-regulated DEGs is mainly associated with immune response (B), MET (C), and angiogenesis (D). RT-qPCR validation of representative DEGs in ovarian stroma.

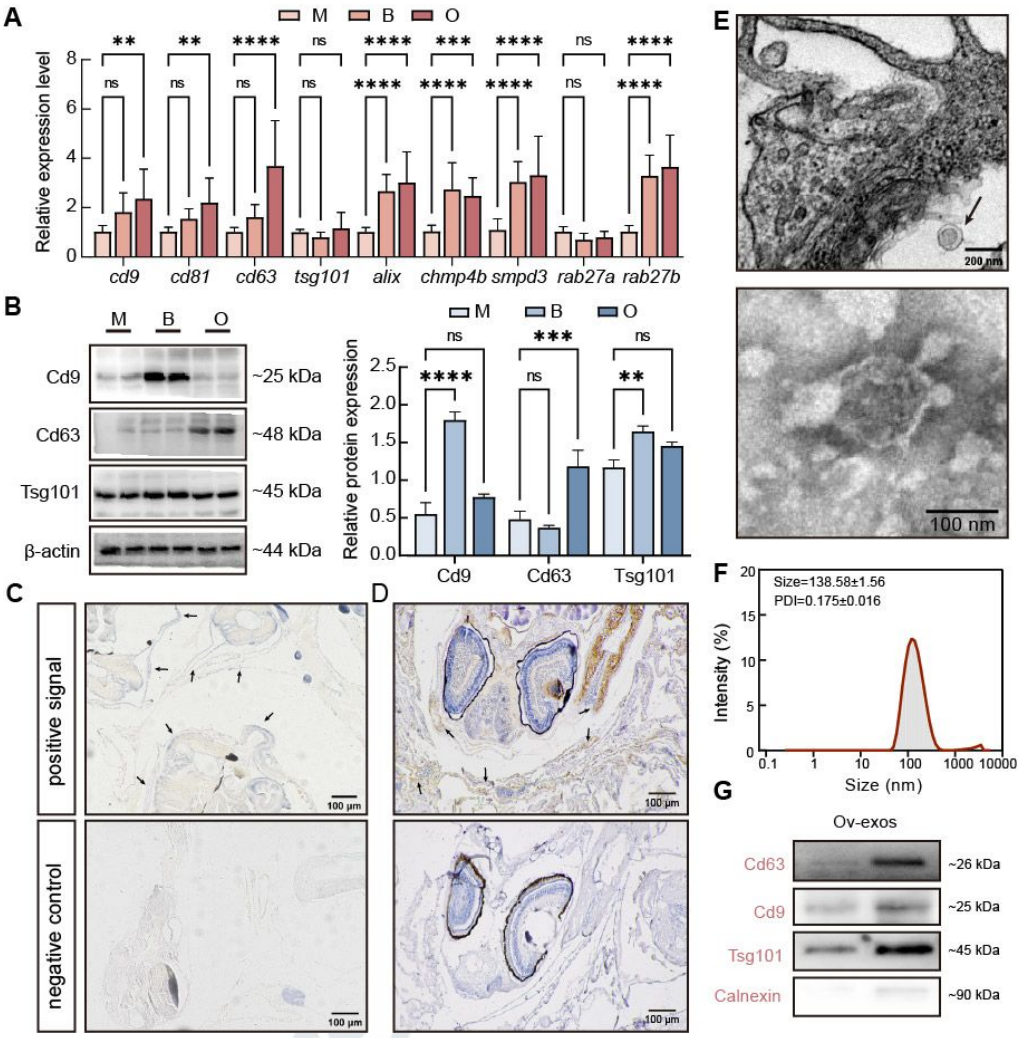

Figure 4. Ov-exos potentially serve as messengers in placental analogue formation

A: RT-qPCR analysis of the relative expression levels of exosome-related genes in ovarian stroma across three stages (n = 3). B: Representative immunoblot and corresponding quantification of relative protein expression in three stages ($n = 3$). C: Localization of *cd63* mRNA in ovary (at pre-hatching phase). Positive signals with antisense probes are shown in blue (indicated by black arrowheads). D: IHC detection of the spatial distribution of Cd63 in the ovary during gestation. Positive signals appear yellow-brown (indicated by black arrowheads), sections were counterstained blue with hematoxylin. E: Electron micrographs of ov-exos located within the placental analogue

(upper, indicated by white arrowheads) and those isolated from the ovary (lower). F: Histogram of a DLS analysis of ov-exos shows the relationship between particle numbers (y-axis) and diameter (x-axis). G: Western blot to detect the expression of Cd63, Cd9, Tsg101 in ov-exos. Values represent mean±SEM. ns, Not Significant; **: P<0.01, ***: P<0.001, ****: P<0.0001; one-way ANOVA followed by Dunnett's test. Scale bars: 200 μm (E, upper), 100 μm (C and D).

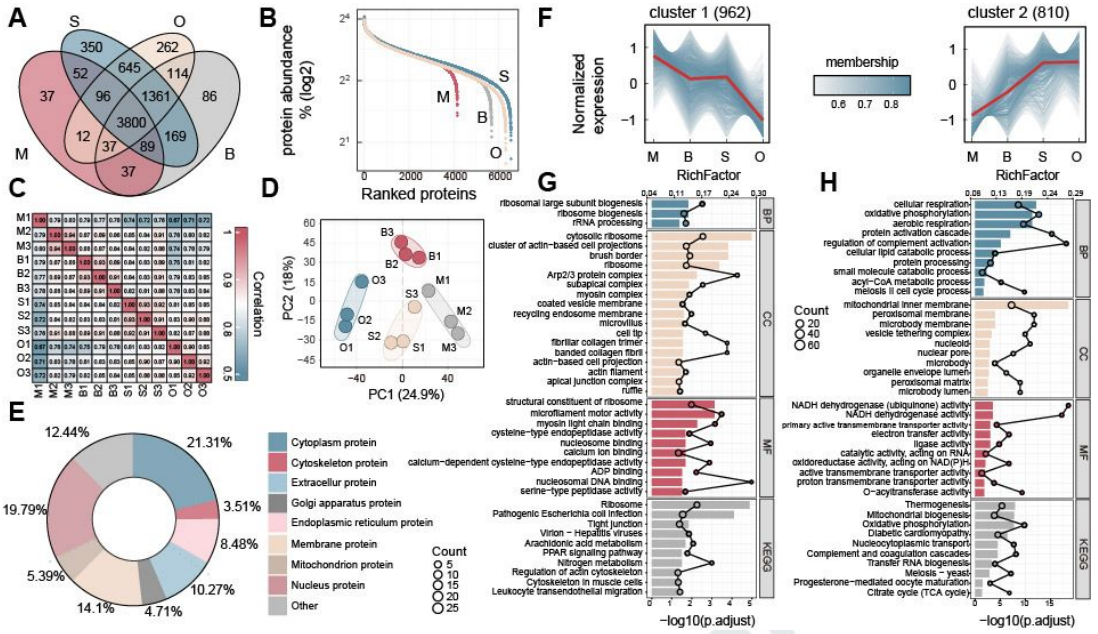

Figure 5. Temporal profiles of ov-exos DEPs and functional enrichment

A: Venn diagram of ov-exos proteins identified across the four groups. B: Ranked abundance of ov-exos proteins in the four groups, showing distribution patterns by relative abundance. C: Principal component analysis (PCA) plot of all samples. D: Correlation heatmap among samples. E: Subcellular localization of ov-exos proteins and their proportions in each category. F: Mfuzz clustering of DEPs identified two clusters with distinct temporal patterns. G–H: Representative enrichment results of target genes of upregulated (G) and downregulated (H) DEPs.

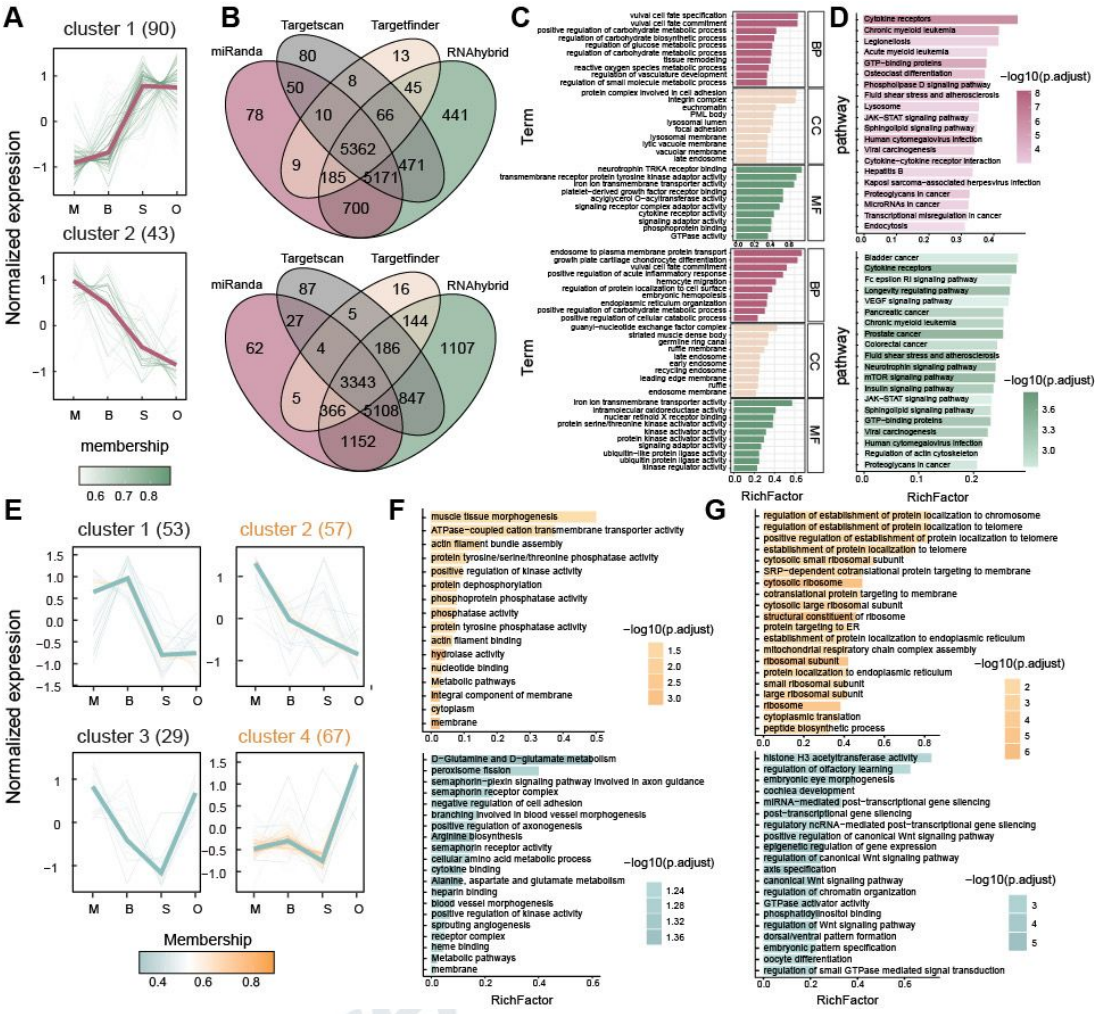

Figure 6. Temporal profiles of ov-exos DEMs/DELs and functional enrichment of target genes

A: Mfuzz clustering of DEMs revealed two clusters exhibiting distinct temporal patterns. B: Venn diagram of DEMs target genes predicted by four algorithms, with colors indicating the respective methods. The intersecting target genes were subjected to GO and KEGG enrichment analyses, and representative results are shown in panels C. The upper panels represent enrichment results of upregulated DEM target genes, and the lower panels represent those of downregulated DEM target genes. D–F: Four clusters of DELs with distinct temporal dynamics were identified by Mfuzz clustering,

followed by representative enrichment results of cis- (E) and trans- (F) acting target genes of DELs.

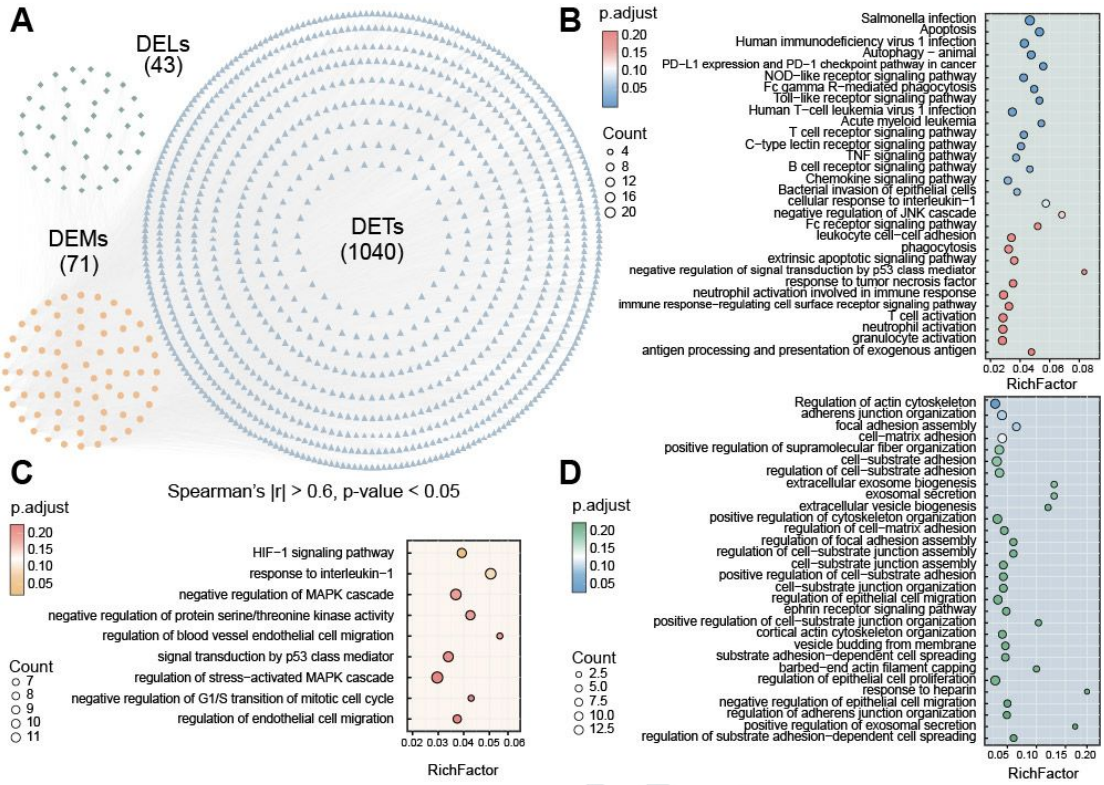

Figure 7. Construction of the ov-exos ceRNA network and enrichment analysis of mRNAs within the network.

A: Overview of the ceRNA network constructed using differentially expressed ov-exos RNAs. Node colors indicate RNA types: mRNAs (blue), miRNAs (yellow), and lncRNAs (green). Functional enrichment analysis of DETs in the network was then performed, highlighting representative pathways related to endothelial cell proliferation and migration (B), lymphocyte-mediated immune response (C), and epithelial tissue morphogenesis (D).

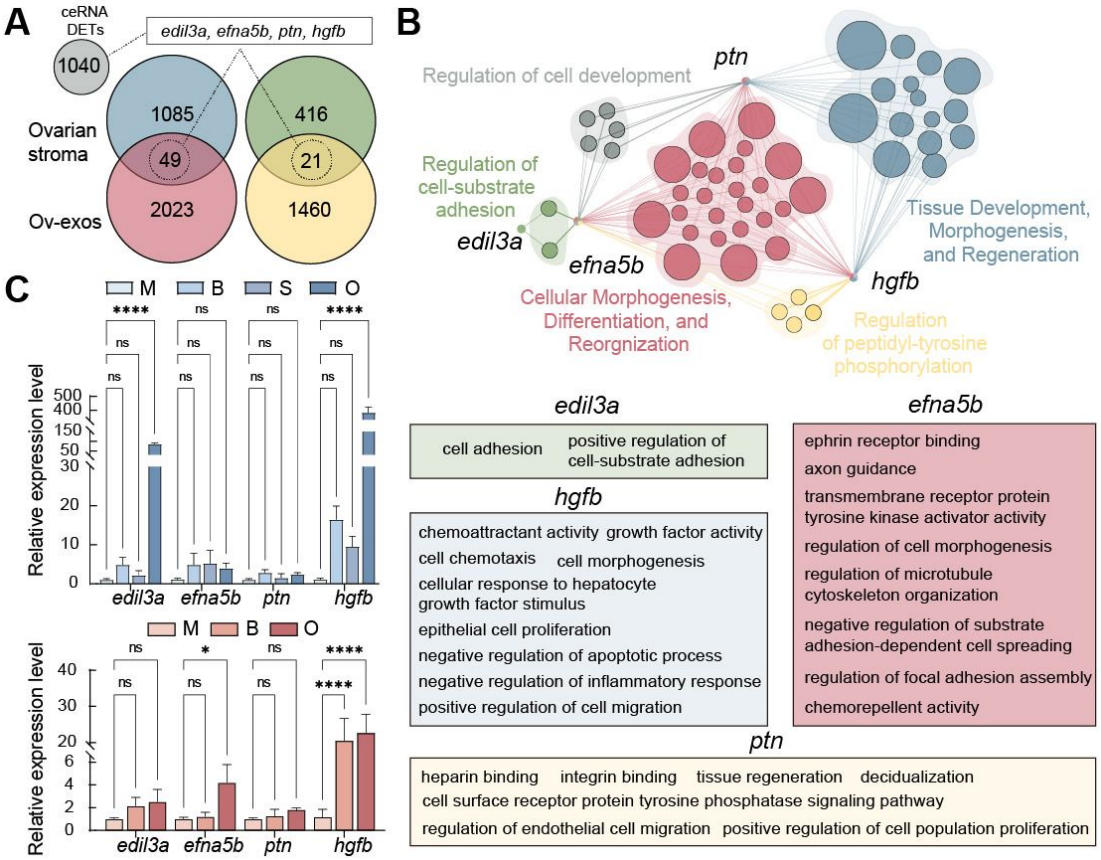

Figure 8. Integrative analysis of ov-exos and ovarian stroma transcriptomes reveals key delivered genes

A: Venn diagram showing the DEGs shared between ov-exos and ovarian stroma, as well as those present in the ceRNA network. B: Enrichment analysis and gene-pathway network analysis of the four candidate genes. C: Relative mRNA expression levels of four candidate genes (*edil3a*, *efna5b*, *hgfb* and *ptn*) were detected by RT-qPCR in ovary (upper) and ov-exos (lower) ($n = 3$). Bars represent mean values±SEM. ns, Not Significant; *: $P< 0.05$, ****: $P< 0.0001$; one-way ANOVA followed by Dunnett's test.

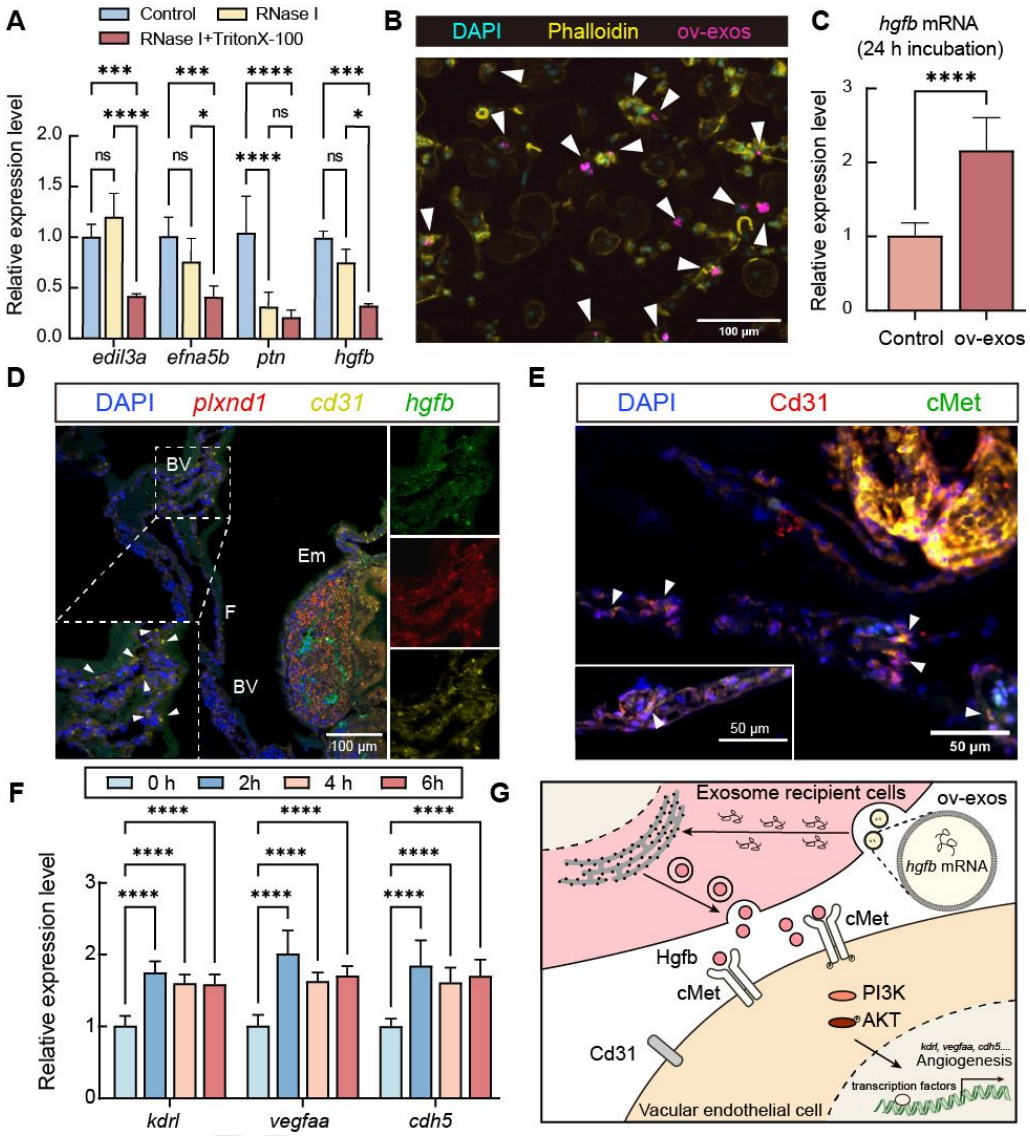

Figure 9. Ov-exos-Mediated *hgfb* mRNAs transfer into ovarian somatic cells

A: RNase I protection assay of exosomal RNAs. The relative expression levels of candidate mRNAs in ov-exos were analyzed by RT-qPCR after treatment with RNase I, with or without Triton X-100 ($n = 3$). B: Representative fluorescence micrographs showing uptake of Exo-Tracker-labeled ov-exos (magenta) by primary ovarian cells. C: Relative mRNA expression levels of *hgfb* were detected by RT-qPCR in primary ovarian cells incubated with or without ov-exos (n = 3). D: DISH images of vascular endothelial cells in black rockfish ovary showing colocalization of *hgfb* (green, Alexa

Fluor 488), *plxnd1* (red, Alexa Fluor 594), and *cd31* (yellow, Alexa Fluor 647). White arrowheads indicate positive colocalization signals. E: Co-localization of Cd31 and cMet in the maternal component of the placental analogue was assessed by IHC. F: RT-qPCR analysis the relative expression levels of three angiogenic genes in ovarian vascular cells treated with rHgfb or PBS (n = 3). G: Schematic illustration of ov-exos delivering hgfb mRNA to recipient cells, subsequently enhancing the synthesis and secretion of HGFB protein and promoting angiogenesis. Bars represent mean values±SEM. ns, Not Significant; *: $P<0.05$, ***: $P<0.001$, ****: $P<0.0001$; one-way ANOVA followed by Dunnett's test. Scale bars: 100 μm (B, D), 50 μm (E).

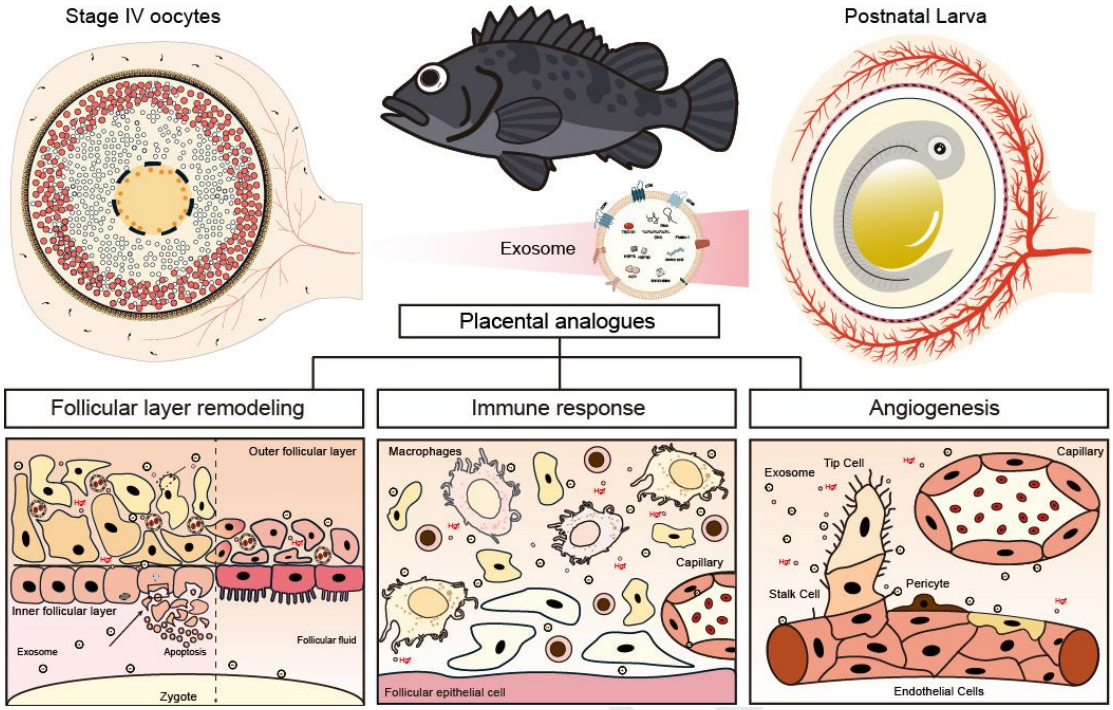

Graph abstract. Ovarian exosomes drive the transformation of follicular tissue into a functional placental analogue during gestation in black rockfish

Supplementary Materials

Supplementary Figures

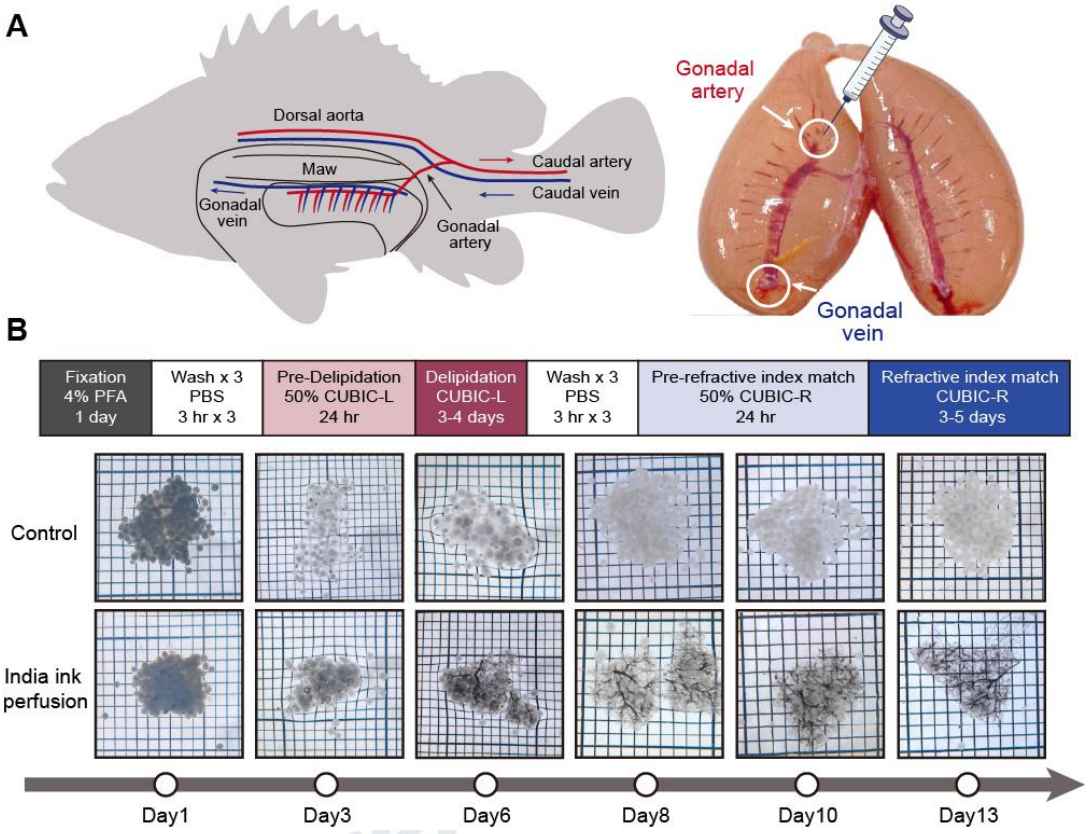

Supplementary Figure S1. Visualization of the ovarian vasculature in black rockfish using vascular perfusion and tissue clearing

A: Schematic diagram of the major vasculature, including ovarian arteries and ovarian veins. B: Steps and representative images of ovarian vascular system visualization via tissue clearing, showing both the control group and the India ink-gelatin perfused group.

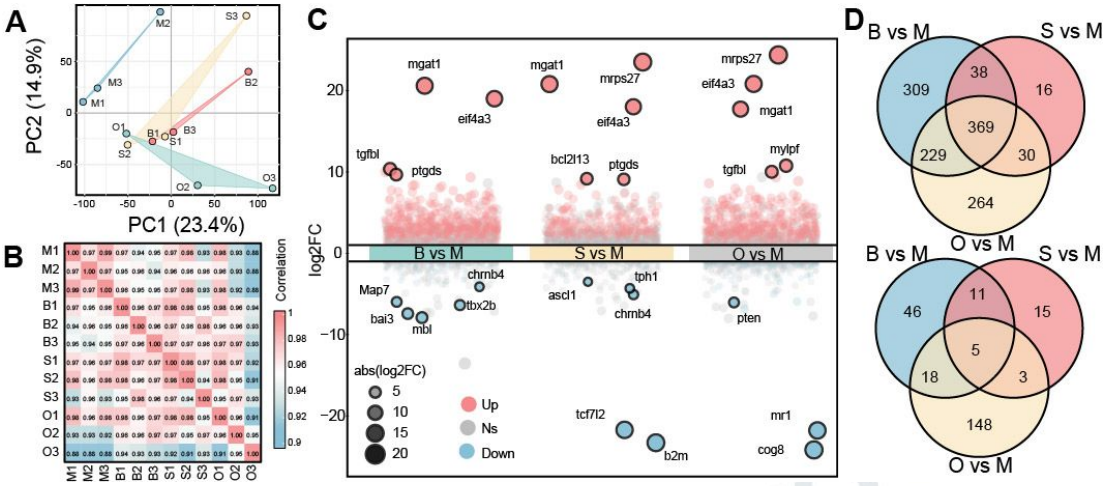

Supplementary Figure S2. RNA-seq profile of black rockfish pre-fertilized and post-fertilized ovary stroma.

A: PCA plot of the 12 samples. B: Correlation heatmap among 12 samples. C: Volcano plots represent the DEGs in three comparsion groups. D: Venn diagram showing upregulated (upper) and downregulated (lower) DEGs across three groups.

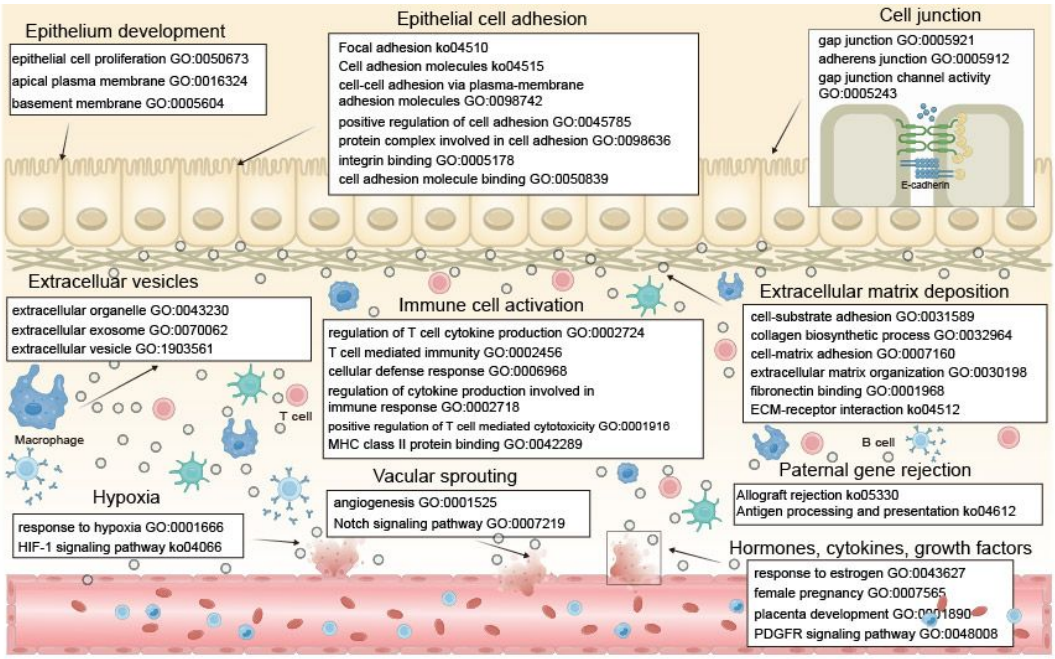

Supplementary Figure S3. Overview of significantly enriched pathways of ovarian stroma DEGs related to the formation of the placental analogue.

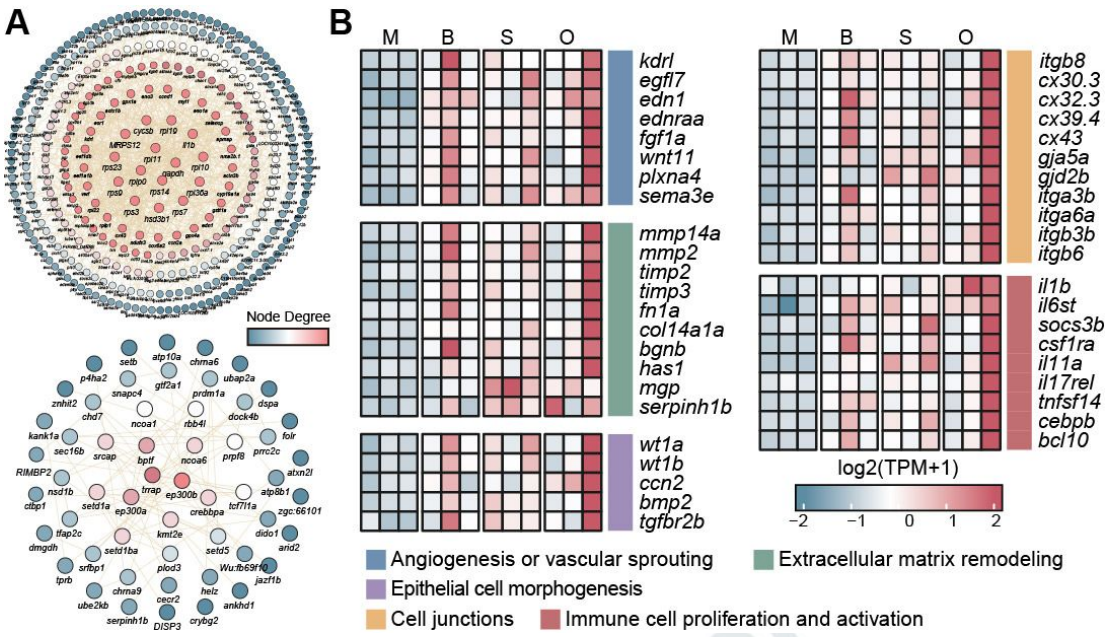

Supplementary Figure S4. PPI network of continuously up- or downregulated DEGs and heatmap of representative genes related to placental analogue development. A: PPI network of continuously upregulated (upper) or downregulated (lower) DEGs, with color depth representing the protein degree score. B: Heatmap of representative DEGs associated with the formation of the placental analogue. Different functional categories are indicated by distinct colored blocks.

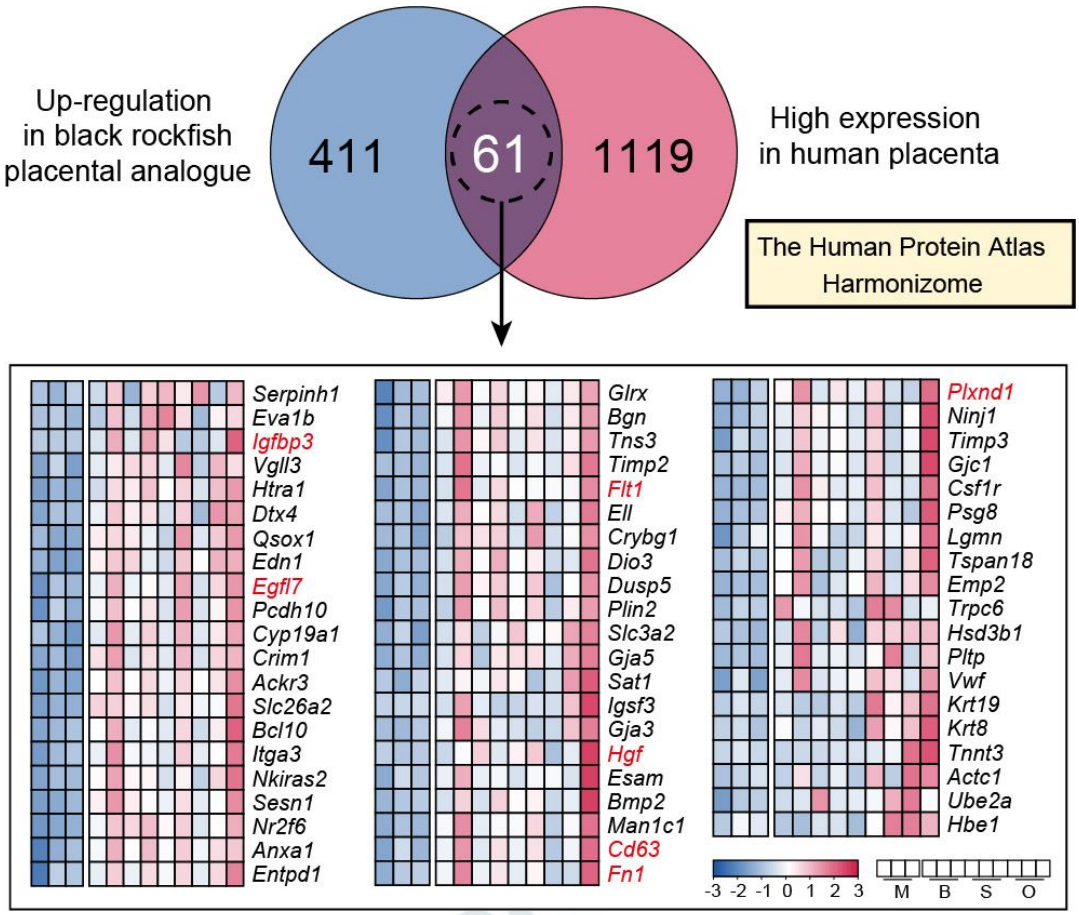

Supplementary Figure S5. Intersection between upregulated DEGs in the placental analogue of black rockfish and highly expressed genes in the human placenta (Diamant et al., 2025; Fagerberg et al., 2014; Rouillard et al., 2016; Uhlén et al., 2015). The heatmap shows the expression patterns of these shared genes in the ovarian stroma of black rockfish.

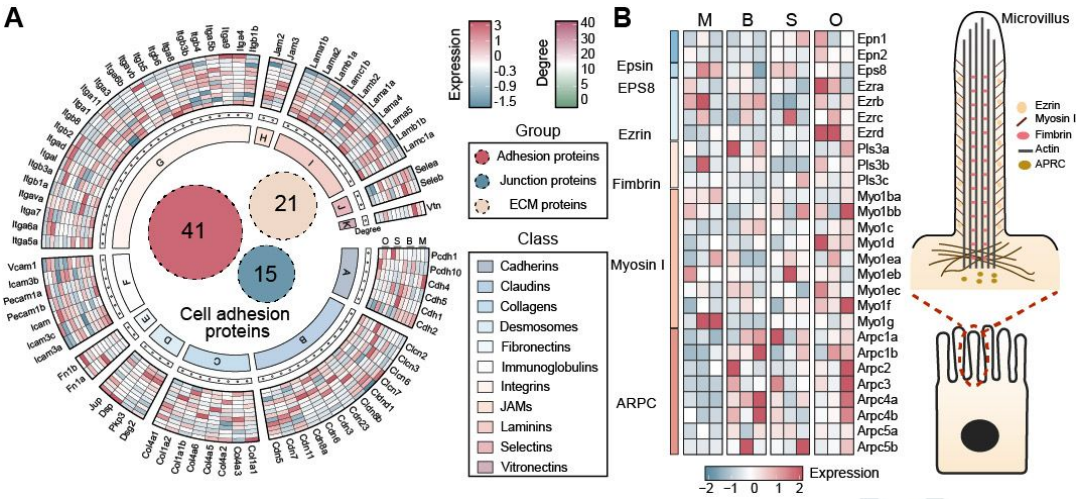

Supplementary Figure S6. Expression profiles of ov-exos proteins associated with cell junctions and microvilli assembly

A: Heatmap of ov-exos proteins involved in cell adhesion, along with a display of PPI degree. B: Heatmap of exos proteins related to microvillus assembly.

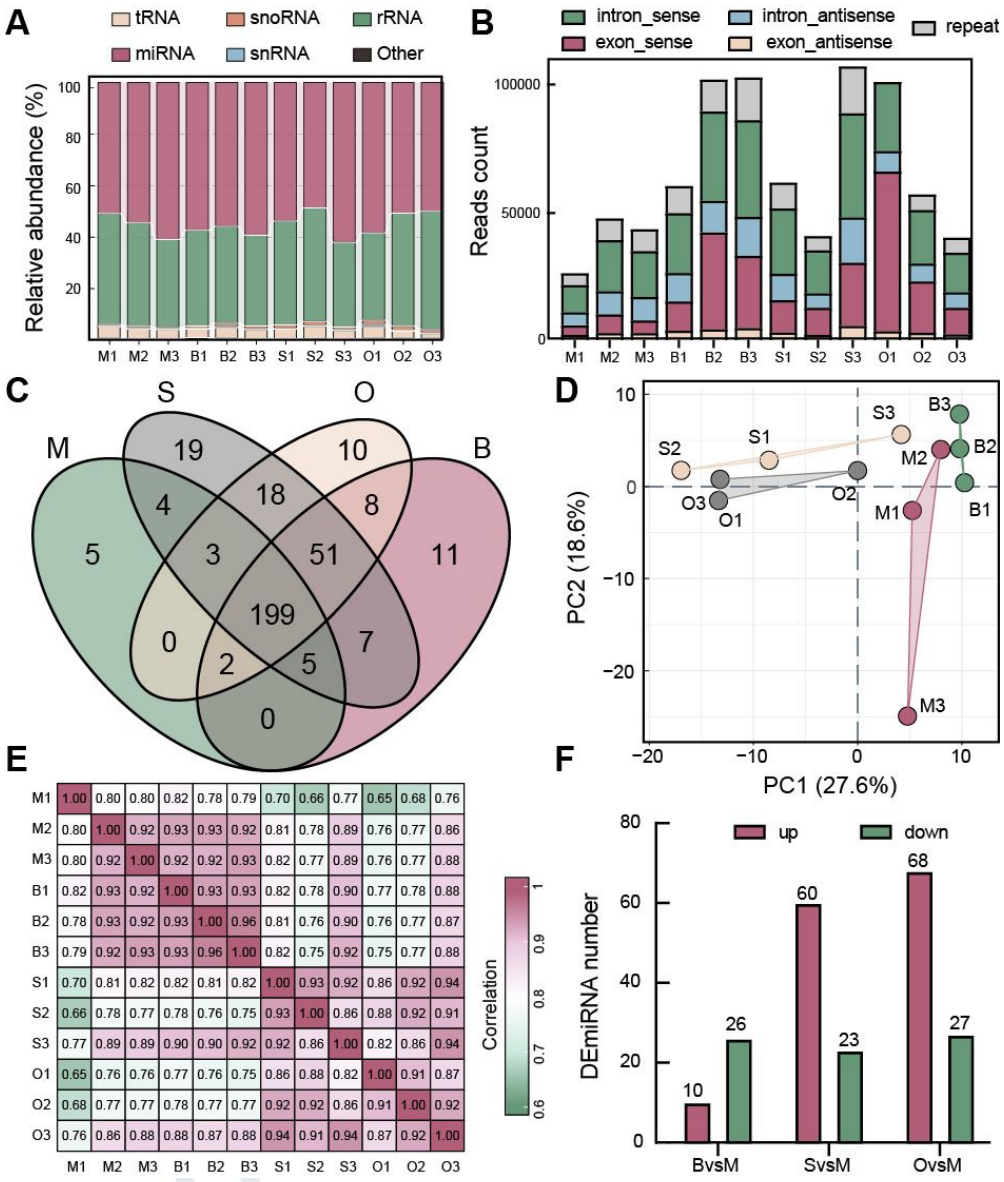

Supplementary Figure S7. SmallRNA-seq profile of black rockfish ov-exos.

A: Classification of small RNAs in ov-exos, showing miRNAs as the most abundant, followed by rRNAs. B: Alignment of reads to exons, introns, and repeat sequences. C: Venn diagram of ov-exos miRNAs identified across the four groups. D: PCA plot of the 12 samples. E: Correlation heatmap among samples. F: Number of DEMs across three comparison groups.

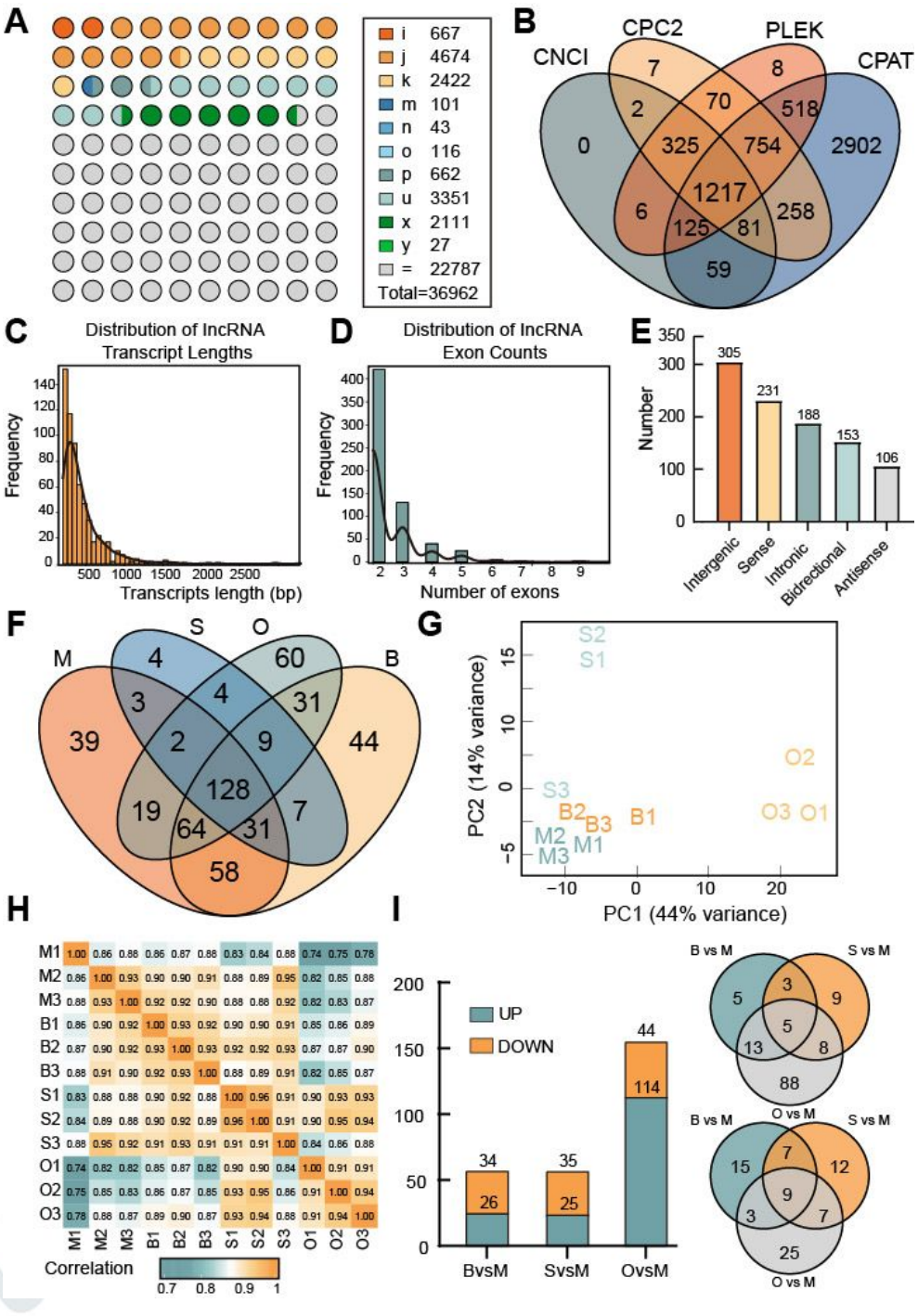

Supplementary Figure S8. LncRNA-seq profile of black rockfish ov-exos.

A: Transcript assembly and identification of novel transcripts (based on gffcompare official guidelines: https://ccb.jhu.edu/software/stringtie/gffcompare.shtml). B: Venn diagram showing novel transcript coding potential predicted by four algorithms. C: Length distribution of lncRNAs. D: Genomic location distribution of lncRNAs. E:

Classification of ov-exos lncRNAs and their proportions in each category. F: Venn diagram of ov-exos lncRNAs identified across the four groups. G: PCA plot of the 12 samples. H: Correlation heatmap among samples. I: Number of DELs across three groups.

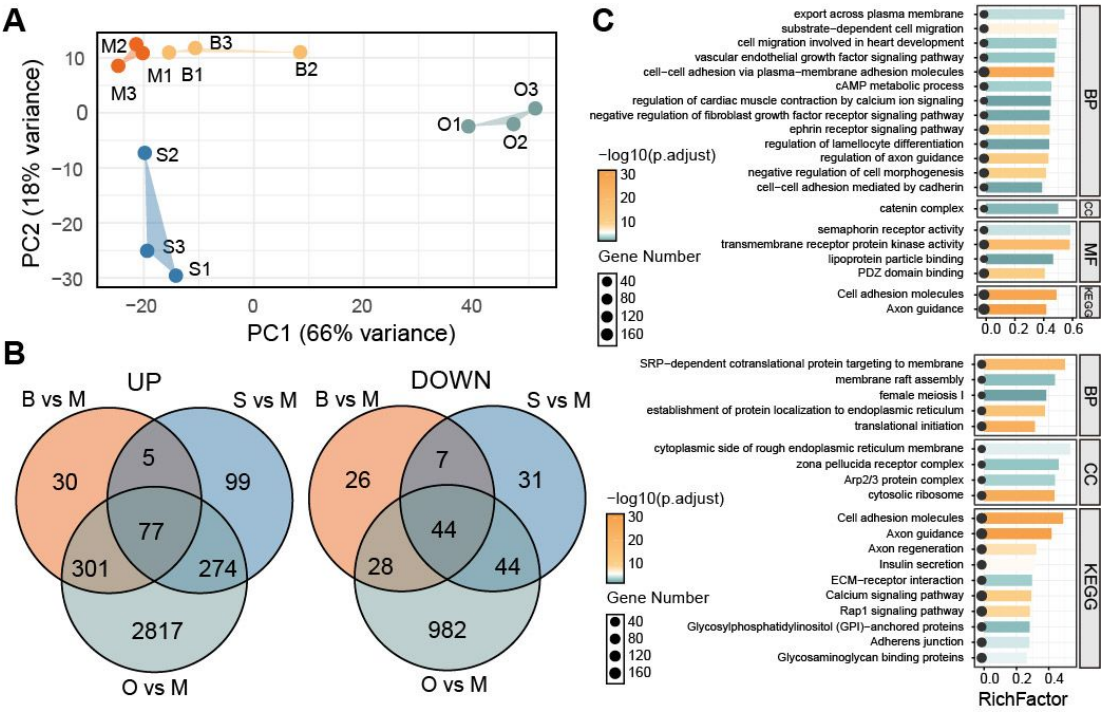

Supplementary Figure S9. Identification and functional enrichment of DETs in ov-exos.

A: PCA plot of all samples. B: Venn diagram showing upregulated (left) and downregulated (right) DETs across three groups. C: Representative enrichment results of upregulated (upper) and downregulated (lower) DETs.

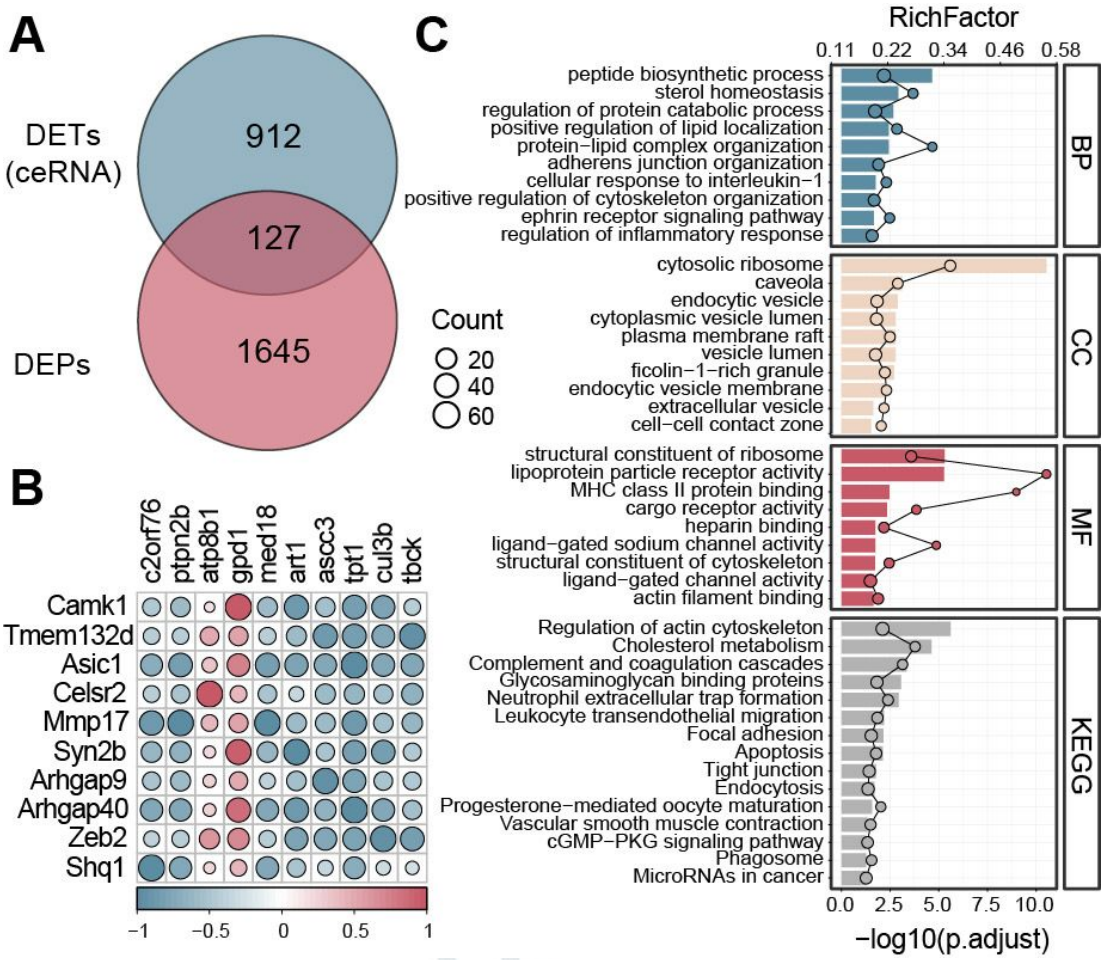

Supplementary Figure S10. Correlation and enrichment analysis of DETs and DEPs in ov-exos.

A: Overlap of geneids of ov-exos DEPs and DETs. B: Correlation heatmap of representative DEPs and DETs. C: Functional enrichment analysis of highly correlated DEPs and DETs.

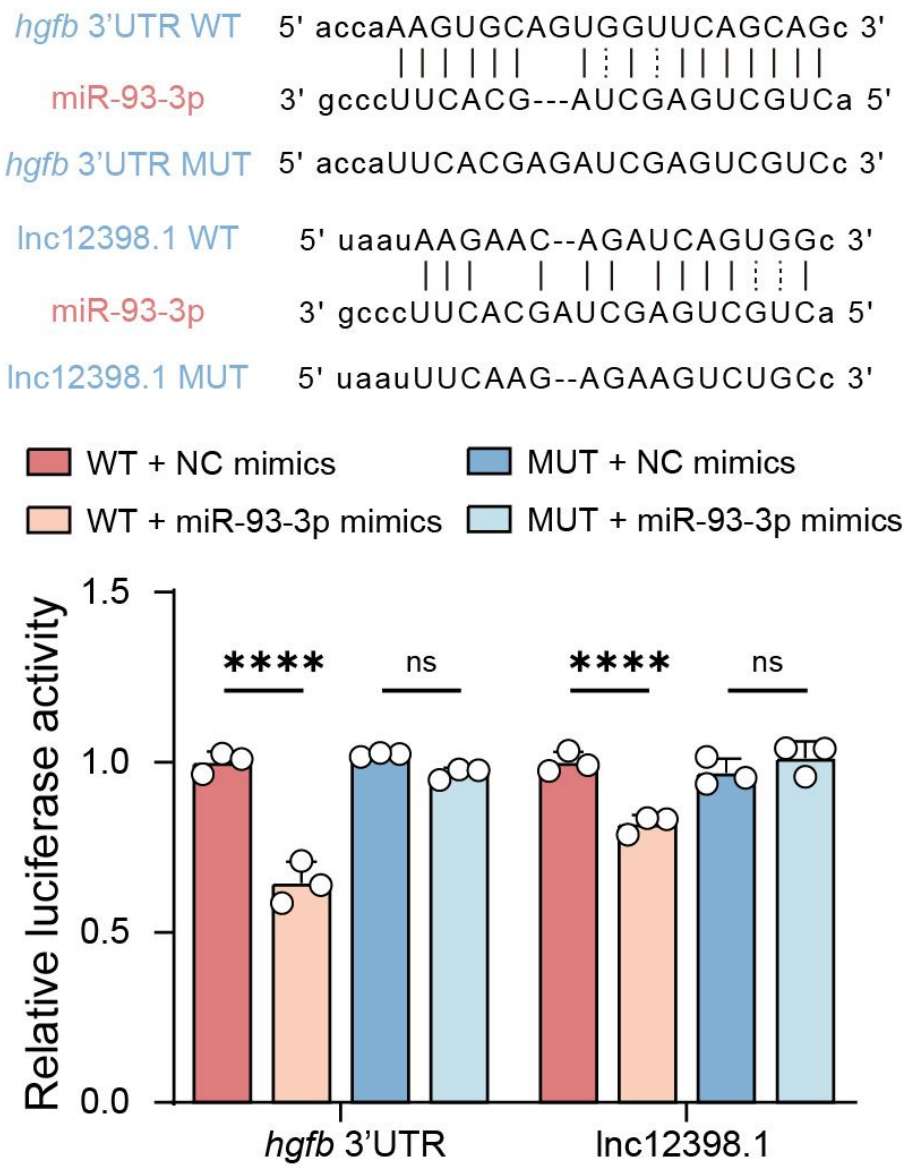

Supplementary Figure S11. Dual-luciferase reporter assay for validation of mRNA-miRNA-lncRNA regulatory networks.

Binding sites were predicted between miR-93-3p and the hgfb 3'UTR, as well as between miR-93-3p and lnc12398.1 (upper panel). The relative luciferase activity in 293 T cells co-transfected with wild-type (WT) or mutant (MUT) binding site vectors of *hgfb* 3' UTR and lnc12398.1 in the presence of miR-93-3p mimics or a negative control (NC) (lower panel). Values represent mean±SEM. ns, Not Significant; ****: $P<0.0001$; one-way ANOVA followed by Dunnett's test.

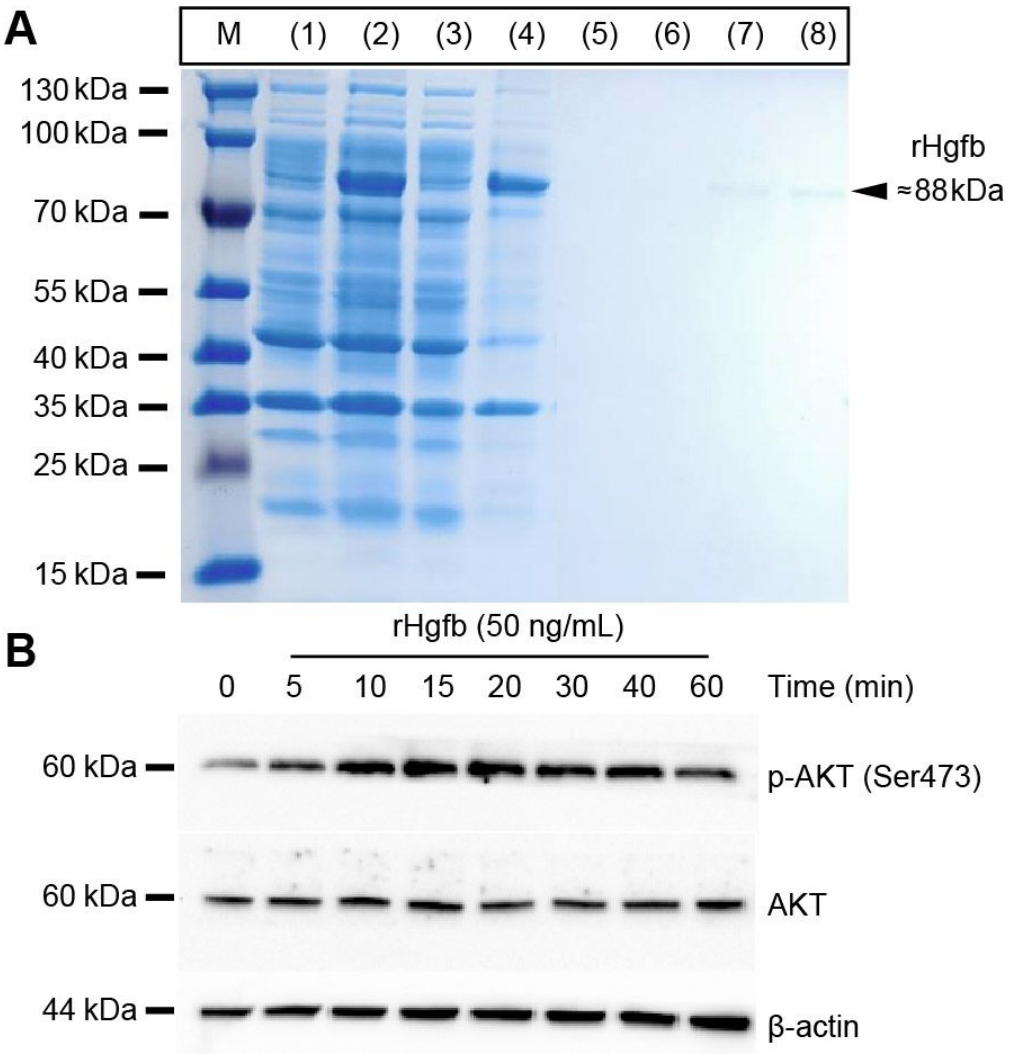

Supplementary Figure S12. Preparation and activity verification of recombinant Hgfb with C terminal His-tag.

A: Prokaryotic expression and purification, M: molecular weight standard. sample (1)-(2) E. coli before and after IPTG induction. (3)–(4) supernatant and pellet separated from lysate of IPTG induced E. coli. (5) Flow-through; (6) washing liquid (40 mM imidazole); (7) elution liquid with purified rHgfb (250 mM imidazole); (8) rHgfb after ultrafiltration-based concentration. B: Primary ovarian microvascular cells were incubated with rHgfb for indicated time intervals, and Akt phosphorylation was examined by Western blotting.

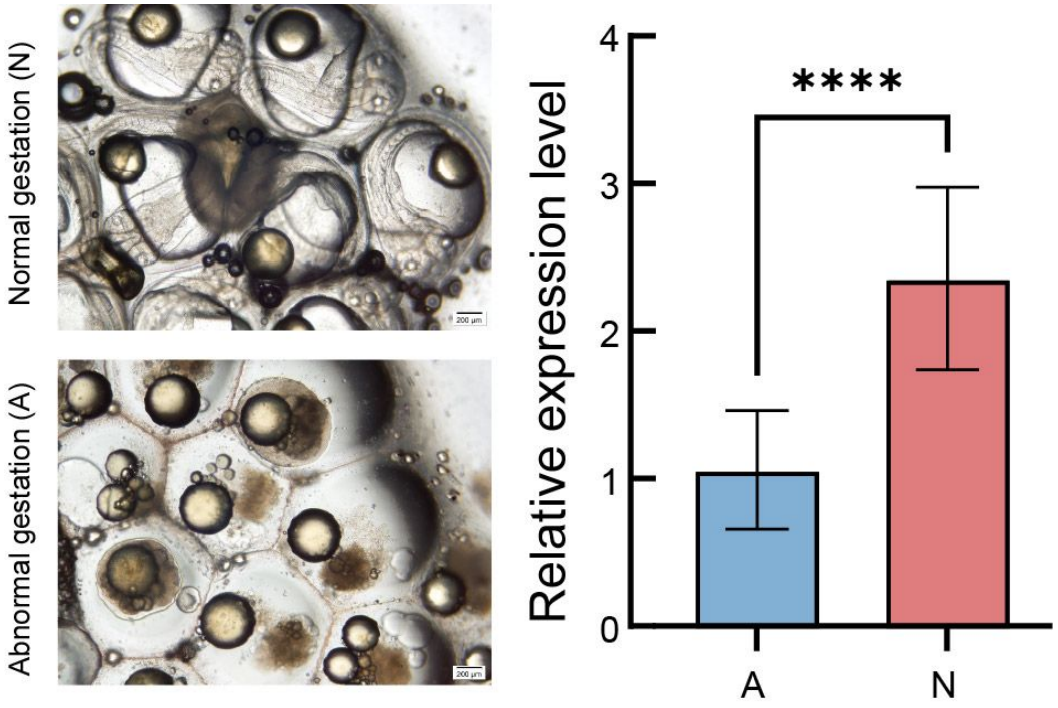

Supplementary Figure S13. In the ovarian stroma, *hgfb* expression is significantly reduced under abnormal gestation compared with normal gestaion.

Upper left: embryos in the ovary under normal pregnancy. Lower left: embryos in the ovary under abnormal pregnancy. Right: RT-qPCR analysis showing significantly reduced *hgfb* expression under abnormal gestation compared with normal gestaion (n=6). Values represent mean±SEM. ****: P<0.0001; unpaired two-tailed Student's t-test.

Supplementary Tables

Supplementary Table S1. Primers and probes used for RT-qPCR and ISH.

Supplementary Table S2. Summary statistics of ovarian stroma RNA-seq data.

Supplementary Table S3. Information on continuously upregulated and downregulated DEGs in the ovarian stroma.

Supplementary Table S4. Functional annotation of proteins identified in ov-exos

Supplementary Table S5. Information on continuously upregulated and downregulated DEPs in the ov-exos.

Supplementary Table S6. Reads number of data filtering and annotation statistics for small RNAs.

Supplementary Table S7. Informations on continuously upregulated and downregulated DEMs in the ov-exos.

Supplementary Table S8. Summary statistics of ov-exos lncRNA-seq data.

Supplementary Table S9. Information on continuously upregulated and downregulated DELs in the ov-exos.

Supplementary Table S10. Information on continuously upregulated and downregulated DETs in the ov-exos.

Supplementary Table S11. ceRNA interaction pairs identified in ov-exos.

外泌体介导许氏平鲉（*Sebastes schlegelii*）卵巢组织向功能性胎盘类似物转化的分子机制研究

作者

郑炳言[1]，王孝杰[1,2]，温海深[1]，李昀[1]，李键爽i[1]，杨欣琳[1]，吕里康[1]，齐鑫[1,*].

1. 海水养殖教育部重点实验室，中国海洋大学，青岛 266100，中国

2. 崖州湾创新研究院，热带海洋学院，三亚 572000，中国

摘要

胎生繁殖策略在真骨鱼类中多次独立进化，从而衍生出多样化的母体营养供给模式。在许氏平鲉妊娠期间，胚胎干重持续增加，母胎之间通过胎盘连接结构进行营养物质传递。先前的研究描述了许氏平鲉胎盘类似物的基本形态和进化趋同性，然而其完整的结构体系以及背后的分子机制仍未得到明确解释。在本研究中，我们表明，来源于卵巢滤泡组织的胎盘类似物的母体部分由血管化的外层和具有腺体和分泌功能的内层构成，并形成包裹胚胎的囊状结构。在分子层面，这一转化过程涉及上皮–间充质相互作用、血管生成以及免疫反应。此外，我们在胎盘类似物周围观察到外泌体样结构，表明胚胎与母体之间存在活跃的通讯作用，并可能参与上述变化的调控。我们随后分离并表征了卵巢来源外泌体。外泌体的蛋白质组学和转录组学分析表明其携带丰富的功能性分子，比如 *hgfb* mRNA。我们进一步证明了许氏平鲉原代卵巢基质细胞可以内化外泌体，引起细胞内 *hgfb* mRNA

816 水平增加，并增强了 Hgfb 蛋白的产生和分泌，从而重塑基因表达谱，驱动包括
817 血管生成在内的胎盘发育相关过程。这些研究结果阐明了许氏平鲉妊娠过程中胎
818 盘类似物形成以及血管形成的分子机制，并为理解鱼类从卵生向胎生演化转变过
819 程中所发生的生殖适应提供了重要的理论依据。

820 **关键词：**许氏平鲉；胎盘类似物；细胞通讯；外泌体；外泌体递送物